ICES Report 04-57

A Goal Oriented *hp*-Adaptive Finite Element Method with Electromagnetic Applications. Part I: Electrostatics.

D. Pardo*, L. Demkowicz*, C. Torres-Verdín**, L. Tabarovsky***

*Institute for Computational Engineering and Sciences (ICES)
The University of Texas at Austin
Austin, TX 78712

**Department of Petroleum and Geosystems Engineering
The University of Texas at Austin
Austin, TX 78712

***Baker Atlas, a division of Baker-Hughes
2001 Rankin Road
Houston, TX 77073

Abstract

We describe the development and application of a Finite Element (FE) self-adaptive *hp* goal-oriented algorithm for elliptic problems. The algorithm delivers (without any user interaction) a sequence of optimal *hp*-grids. This sequence of grids minimizes the error of a prescribed *quantity of interest* with respect to the problem size. The refinement strategy is an extension of the fully automatic, energy-norm based, *hp*-adaptive algorithm [9, 17].

We illustrate the efficiency of the method with 2D numerical results. Among other problems, we apply the goal-oriented *hp*-adaptive strategy to simulate direct current (DC) resistivity logging instruments (including Through Casing Resistivity Tools) in a borehole environment and for the assessment of rock formation properties.

1 Introduction

During the last decades, different algorithms intended to generate *optimal* grids for solving relevant engineering problems have been designed and implemented. Among those algorithms, a Finite Element (FE) self-adaptive *hp*-refinement strategy has recently (2001) been developed at the Institute for Computational Engineering and Sciences (ICES) of The University of Texas at Austin. The strategy produces automatically a sequence of *hp*-meshes that delivers *exponential convergence rates* in terms of the *energy-norm* error against the number of unknowns (as well as the CPU time), independently of the number and type of singularities of the problem. Thus, it provides high accuracy approximations of solutions corresponding to a variety of engineering applications. Furthermore, the self-adaptive strategy is *problem independent*, and can be applied to FE discretizations of H^1-, $H(curl)$-, and $H(div)$-spaces, as well as to nonlinear problems (see [9, 17] for details).

However, the energy-norm is a quantity of limited relevance for most engineering applications, especially when a particular objective is pursued, as for example, to simulate the electromagnetic response of a petroleum engineering resistivity logging instrument in a borehole environment. In these instruments, the solution (for example, the electric field) is typically several orders of magnitude smaller at the receiver antennas than at the transmitter antennas. Thus, small relative errors of the solution in the energy-norm *do not* imply small relative errors of the solution at the receiver antennas. Indeed, it is not uncommon to construct adaptive grids delivering a relative error in the energy-norm below 1% while the solution at the receiver antennas still contains an error above 1000% (see [15]).

Consequently, a self-adaptive strategy is needed to approximate a specific feature of the solution. Refinement strategies of this type are called *goal-oriented* adaptive algorithms [13, 16], and are based on minimizing the error of a prescribed *quantity of interest* mathematically expressed in terms of a linear functional (see [5, 11, 14, 13, 16, 18] for details.

In this work, we formulate, implement, and study (both theoretically and numerically) a number of self-adaptive goal-oriented algorithms intended to solve elliptic problems. These algorithms are an extension of the fully automatic (energy-norm based) *hp*-adaptive strategy described in [9, 17], and a continuation of concepts presented in [21]. Several 2D applications, including simulation of a logging Through Casing Resistivity Tool (TCRT) [12, 19], illustrate the efficiency and performance of the goal-oriented *hp*-adaptive strategy.

The organization of this document is as follows. In Section 2, we introduce the steady-state Maxwell's equations, which are the governing equations of our DC resistivity logging applications of interest. A family of goal-oriented h and hp self-adaptive algorithms for elliptic problems are presented in Section 3. The corresponding details of implementation are discussed in the same Section. In section 4, we describe our logging DC applications of

interest. Simulations and numerical results for these applications are shown in Section 5. Finally, in Section 6 we draw the main conclusions, and outline future lines of research.

This paper also contains three appendices. In appendix A, we derive the exact solution of two problems used for testing purposes: radiation of a point source into a homogeneous medium, and through casing. In appendix B, we describe a postprocessing formula to extract point values from a Finite Element (FE) solution. Finally, Appendix C contains numerical 2D results that compare the efficiency of each of the self-adaptive algorithms, and describe the corresponding final h or hp-grids.

2 Maxwell's Equations

2.1 Time-harmonic Maxwell's equations

Assuming a time-harmonic dependence of the form $e^{j\omega t}$, with ω denoting the angular frequency, Maxwell's equations can be written as

$$\begin{cases} \boldsymbol{\nabla} \times \boldsymbol{H} &= (\sigma + j\omega\epsilon)\boldsymbol{E} + \boldsymbol{J} & \text{Ampere's Law,} \\ \boldsymbol{\nabla} \times \boldsymbol{E} &= -j\omega\mu\, \boldsymbol{H} & \text{Faraday's Law,} \\ \boldsymbol{\nabla} \cdot (\epsilon \boldsymbol{E}) &= \rho & \text{Gauss' Law of Electricity, and} \\ \boldsymbol{\nabla} \cdot (\mu \boldsymbol{H}) &= 0 & \text{Gauss' Law of Magnetism.} \end{cases} \tag{2.1}$$

Here $\boldsymbol{H}$ and $\boldsymbol{E}$ denote the magnetic and electric field, respectively, $\boldsymbol{J}$ is a prescribed, impressed current source, ϵ, μ, and σ stand for dielectric permittivity, magnetic permeability, and electrical conductivity of the medium, respectively, and ρ denotes the electric charge distribution.

The equations described in (2.1) are to be understood in the distributional sense, i.e. they are satisfied in the classical sense in subdomains of regular material data, but they also imply appropriate interface conditions across material interfaces.

Energy considerations lead to the assumption that both electric field $\boldsymbol{E}$ and magnetic field $\boldsymbol{H}$ must be square integrable. This is not true for the charge distribution which may include irregular (Dirac's type) terms corresponding to surface charges accumulated over material interfaces. Similarly, the impressed current may be an irregular distribution including surface currents contributions.

Maxwell's equations are not independent. Taking the curl of Faraday's Law yields the Gauss' Law of magnetism. By taking the curl of Ampere's Law, and by utilizing Gauss'

Electric Law we arrive at the so called continuity equation,

$$\boldsymbol{\nabla} \cdot (\sigma \boldsymbol{E}) + j\omega\rho + \boldsymbol{\nabla} \cdot \boldsymbol{J} = 0\,. \tag{2.2}$$

Maxwell's equations are to be satisfied in the whole space minus domains occupied by perfect conductors. A perfect conductor is an idealization of highly conductive media. In a region where $\sigma \to \infty$, the corresponding electric field converges to zero. Faraday's law implies that the tangential component of the electric field $\boldsymbol{E}$ must remain continuous across material interfaces. Consequently, the tangential component of electric field must vanish along the Perfect Electric Conductor (PEC) boundary. The same Faraday's law implies that the normal component of the magnetic field on the PEC boundary must vanish. The subdomains occupied by PEC are eliminated from the solution domain and replaced with the PEC boundary conditions, namely,

$$\boldsymbol{n} \times \boldsymbol{E} = \boldsymbol{0}, \quad \boldsymbol{n} \cdot \boldsymbol{H} = 0\,. \tag{2.3}$$

The tangential component of magnetic field (surface current) and normal component of the electric field need not be zero, and may be determined a-posteriori.

2.2 Steady State Maxwell's equations

At Direct Current (DC, *i.e.*, $\omega = 0$), the time-harmonic Maxwell's equations reduce to,

$$\begin{cases} \boldsymbol{\nabla} \times \boldsymbol{H} & = \sigma \boldsymbol{E} + \boldsymbol{J} & \text{Ampere's Law,} \\ \boldsymbol{\nabla} \times \boldsymbol{E} & = 0 & \text{Faraday's Law,} \\ \boldsymbol{\nabla} \cdot (\epsilon \boldsymbol{E}) & = \rho & \text{Gauss' Law of Electricity, and} \\ \boldsymbol{\nabla} \cdot (\mu \boldsymbol{H}) & = 0 & \text{Gauss' Law of Magnetism.} \end{cases} \tag{2.4}$$

Similarly, the continuity equation reduces to,

$$\boldsymbol{\nabla} \cdot (\sigma \boldsymbol{E}) + \boldsymbol{\nabla} \cdot \boldsymbol{J} = 0\,. \tag{2.5}$$

For simplicity, we shall assume that the solution domain is simply connected. Faraday's law implies that there exists a scalar potential u such that,

$$\boldsymbol{E} = -\boldsymbol{\nabla} u\,. \tag{2.6}$$

The continuity law (here understood in the distributional sense) implies that, in the subdomain occupied by conductive media, the potential must satisfy the so called *conductive media equation*, *i.e.*,

$$\boldsymbol{\nabla} \cdot (\sigma \boldsymbol{\nabla} u) = -\boldsymbol{\nabla} \cdot \boldsymbol{J}\,, \tag{2.7}$$

accompanied by homogeneous[1] Neumann boundary condition on the conductive/non-conductive material interface,

$$\sigma \frac{\partial u}{\partial n} = 0 \,. \tag{2.8}$$

The PEC boundary condition $\boldsymbol{n} \times \boldsymbol{E} = \boldsymbol{0}$ implies that the potential must be constant along each connected component of the PEC boundary. If the PEC boundary is connected, we may assume that the constant is equal zero. This results in the homogeneous Dirichlet boundary condition,

$$u = 0 \,. \tag{2.9}$$

Once the solution in the conductive region has been determined, the potential in the non-conductive part of the domain can be determined by solving the *electrostatics equation*,

$$-\boldsymbol{\nabla} \cdot (\epsilon \boldsymbol{\nabla} u) = \rho \,, \tag{2.10}$$

resulting from Gauss' Electric Law, accompanied by the Dirichlet boundary condition $u = u_0$ on the non-conductive region boundary. Here u_0 is constant on a PEC boundary and equal to the solution in the conductive region on the conductive/non-conductive interface. The charge ρ must be known a priori.

In this paper, we focus our attention to the solution of the conductive media equation in the conductive region only.

2.3 Variational Formulation

By multiplying equation (2.7) by test function $\xi \in H^1(\Omega)$, and by integrating by parts over the domain Ω, we obtain the following variational formulation:

$$\begin{cases} \text{Find } u \in H^1(\Omega) \text{ such that:} \\ \displaystyle\int_\Omega \sigma \nabla u \nabla \xi \; dV = \int_\Omega \nabla \cdot \mathbf{J} \; \xi \; dV + \int_{\partial\Omega} \sigma \frac{\partial u}{\partial n} \xi \; dS \quad \forall \xi \in H^1(\Omega) \,, \end{cases} \tag{2.11}$$

where $H^1(\Omega) = \{u \in L^2(\Omega) \; : \nabla u \in L^2(\Omega)\}$ is the *space of admissible solutions* (potentials). Notice that solution of problem (2.11) is not unique. In order to obtain a unique solution, we introduce an essential (Dirichlet) boundary condition (BC) in some region Γ_D of the

[1] Unless the normal component of the impressed current is discontinuous across the material interface. In such a case, $\sigma \frac{\partial u}{\partial n} = [\boldsymbol{n} \cdot \boldsymbol{J}]$ where $[\boldsymbol{n} \cdot \boldsymbol{J}]$ denotes the jump of the normal component of $\boldsymbol{J}$

computational domain Ω. At this point, we also introduce a natural (Neumann) boundary condition (BC) in some region Γ_N of the computational domain Ω. It then follows that:

$$\left\{ \begin{array}{l} \text{Find } u \in u_D + H^1_D(\Omega) \text{ such that:} \\ \int_\Omega \sigma \nabla u \nabla \xi \, dV = \int_\Omega \nabla \cdot \mathbf{J} \, \xi \, dV + \int_{\Gamma_N} g \, \xi \, dS \quad \forall \xi \in H^1_D(\Omega) \, , \end{array} \right. \tag{2.12}$$

where $\mathbf{n}$ is the unit normal outward (with respect Ω) vector, u_D is a lift (typically $u_D = 0$) of the essential boundary condition data u_D (denoted with the same symbol), $g = \sigma \dfrac{\partial u}{\partial n}$ is a prescribed flux on Γ_N, and $H^1_D(\Omega) = \{u \in L^2(\Omega) \ : u|_{\Gamma_D} = 0 \, , \nabla u \in L^2(\Omega)\}$ is the space of admissible test functions associated with problem (2.12).

2.4 Cylindrical Coordinates and Axisymmetric Problems

Using cylindrical coordinates (ρ, ϕ, z), problem (2.12) becomes:

$$\left\{ \begin{array}{l} \text{Find } u \in u_D + V \text{ such that:} \\ \int_\Omega \sigma \nabla u \nabla \xi \, \rho \, d\rho d\psi dz = \int_\Omega \nabla \cdot \mathbf{J} \, \xi \, \rho \, d\rho d\psi dz + \int_{\Gamma_N} g \, \xi \, dS \quad \forall \xi \in V \, , \end{array} \right. \tag{2.13}$$

where $V = \{u : \Omega \to R \ : u|_{\Gamma_D} = 0 \, , \ \int |u|^2 \rho \, d\rho dz < \infty \, , \ \int (|\dfrac{\partial u}{\partial \rho}|^2 + |\dfrac{\partial u}{\partial z}|^2) \, \rho \, d\rho dz < \infty\}$. Notice that the Jacobian dS of the surface integral in terms of cylindrical coordinates depends upon the particular surface S under consideration.

For the Petroleum Engineering applications entertained in this paper, we assume that both the logging instrument and the rock formation are axisymmetric (invariant with respect to the azimuthal component ϕ). Under this assumption, and dividing (2.13) by a factor of 2π, we derive the following formulation in terms of cylindrical coordinates (ρ, z):

$$\left\{ \begin{array}{l} \text{Find } u \in u_D + V \text{ such that:} \\ \int_\Omega \sigma \rho (\dfrac{\partial u}{\partial \rho}\dfrac{\partial \xi}{\partial \rho} + \dfrac{\partial u}{\partial z}\dfrac{\partial \xi}{\partial z}) \, d\rho dz = \int_\Omega (\dfrac{\partial (\rho J_\rho)}{\partial \rho} + \rho \dfrac{\partial J_z}{\partial z}) \, \xi \, d\rho dz + \int_{\Gamma_N} \sigma \dfrac{\partial u}{\partial n} \xi \, dl \, . \end{array} \right. \tag{2.14}$$

Remark 1. At the axis of symmetry ($\rho = 0$), no BC should be added since there is no boundary in the original 3D problem. From the computational point of view, this effect can be achieved by artificially *adding* a homogeneous natural (Neumann) BC. ∎

3 Goal-Oriented Adaptivity

We are interested in solving the variational problem (2.14), that we state here in terms of bilinear form b, and linear form f:

$$\begin{cases} \text{Find } u \in u_D + V \\ b(u,v) = f(v) \quad \forall v \in V \ . \end{cases} \tag{3.15}$$

Here

- u_D is a lift of the essential (Dirichlet) BC data.
- V is a Hilbert space.
- $f \in V'$ is a linear and continuous functional on V.
- b is a bilinear and symmetric form (assumed to be coercive and continuous in the space V). Thus, we can define an inner product on V as $(u,v) := b(u,v)$, with the corresponding norm denoted by $\|u\|$.

Given an *hp*-FE subspace $V_{hp} \subset V$, we discretize (3.15) as follows:

$$\begin{cases} \text{Find } u_{hp} \in u_D + V_{hp} \\ b(u_{hp}, v_{hp}) = f(v_{hp}) \quad \forall v_{hp} \in V_{hp} \ . \end{cases} \tag{3.16}$$

The objective of goal-oriented adaptivity is to construct an optimal *hp*-grid, in the sense that it minimizes the problem size needed to achieve a given tolerance error for a given *quantity of interest* $L \in V'$. By recalling the linearity of L, we have:

$$E = L(u) - L(u_{hp}) = L(u - u_{hp}) = L(e) \ , \tag{3.17}$$

where $e = u - u_{hp}$ denotes the error function. By defining the residual $r_{hp} \in V'$ as $r_{hp}(v) = f(v) - b(u_{hp}, v) = b(u - u_{hp}, v) = b(e, v)$, we look for the solution of the *dual problem*:

$$\begin{cases} \text{Find } w \in V \\ b(v,w) = L(v) \quad \forall v \in V \ . \end{cases} \tag{3.18}$$

Using the Lax-Milgram theorem we conclude that problem (3.18) has a unique solution in V. The solution, w, is usually referred to as the *influence function*.

By discretizing (3.18) via, for example, $V_{hp} \subset V$, we obtain:

$$\begin{cases} \text{Find } w_{hp} \in V_{hp} \\ b(v_{hp}, w_{hp}) = L(v_{hp}) \quad \forall v_{hp} \in V_{hp} \ . \end{cases} \tag{3.19}$$

Due to the symmetry of the bilinear form b and the use of the same space V_{hp} for solving both (3.16) and (3.19), it is only necessary to factorize the system of linear equations once. Thus, the extra cost of solving (3.19) reduces to only one backward and forward substitution (if a direct solver is used).

By orthogonality of e with respect to V_{hp} (in the b-inner product), we have $b(e, v_{hp}) = 0$ for all $v_{hp} \in V_{hp}$. Defining $\epsilon = \epsilon(v_{hp}) = w - v_{hp}$, we obtain :

$$E = L(e) = b(e, \epsilon) \ . \tag{3.20}$$

Once the error E in the quantity of interest has been determined in terms of the bilinear form, we wish to obtain a sharp upper bound for $\mid E \mid$ that utilizes only *local and computable* quantities. Then, a self-adaptive algorithm intended to minimize this bound will be defined.

First, using a similar procedure to the one described in [9], we approximate u and w with *fine grid* functions $u_{\frac{h}{2}, p+1}$, $w_{\frac{h}{2}, p+1}$, which have been obtained by solving iteratively the corresponding linear system of equations associated with the FE subspace $V_{\frac{h}{2}, p+1}$. In the remainder of this paper, u and w will denote the fine grid solutions of the direct and dual problems ($u = u_{\frac{h}{2}, p+1}$, and $w = w_{\frac{h}{2}, p+1}$, respectively), and we will restrict ourselves to discrete FE spaces only.

Next, we bound the error in the quantity of interest by a sum of element contributions. Let b_K be defined as $b_K(u_K, v_K) = b(u_K, v_K)$ for all $u_K, v_K \in V_K$, where $V_K \subset V$. It then follows that:

$$\mid E \mid = \mid b(e, \epsilon) \mid \leq \sum_K \mid b_K(e, \epsilon) \mid \ , \tag{3.21}$$

where summation over K indicates summation over elements. The inner product and norm associated with the bilinear form b_K will be denoted as $(\cdot, \cdot)_K$ and $\| \cdot \|_K$, respectively.

Projection based interpolation operator. At this point, we introduce the *projection-based interpolation* operator $\Pi_{hp} : V \longrightarrow V_{hp}$ defined in [8], and used in [9, 17] for the construction of the fully automatic energy-norm based *hp*-adaptive algorithm. We define $P_{hp} : V \longrightarrow V_{hp}$ as the b-projection, and we denote $u_{hp} = P_{hp} u$. Then, (3.21) becomes:

$$\mid E \mid \leq \sum_K \mid b_K(e, \epsilon) \mid = \sum_K \mid b_K(u - \Pi_{hp} u, \epsilon) + b_K(\Pi_{hp} u - P_{hp} u, \epsilon) \mid \ . \tag{3.22}$$

Given an element K, it is expected that $\mid b_K(\Pi_{hp}u - P_{hp}u, \epsilon) \mid$ will be negligible compared to $\mid b_K(u - \Pi_{hp}u, \epsilon) \mid$. Under this assumption, we conclude that:

$$\mid E \mid \preceq \sum_K \mid b_K(u - \Pi_{hp}u, \epsilon) \mid \ . \tag{3.23}$$

In particular, for $\epsilon = w - \Pi_{hp}w$, we have:

$$\mid E \mid \preceq \sum_K \mid b_K(u - \Pi_{hp}u, w - \Pi_{hp}w) \mid \ . \tag{3.24}$$

By applying the parallelogram law to the last equation, we obtain the next upper bound for $\mid E \mid$:

$$\mid E \mid \preceq \frac{1}{4} \sum_K \mid\mid\mid \tilde{e} + \tilde{\epsilon} \mid\mid_K^2 - \mid\mid \tilde{e} - \tilde{\epsilon} \mid\mid_K^2 \mid \ , \tag{3.25}$$

where $\tilde{e} = u - \Pi_{hp}u$, and $\tilde{\epsilon} = w - \Pi_{hp}w$. A second upper bound for $\mid E \mid$ can be obtained from Cauchy-Schwartz inequality as follows:

$$\mid E \mid \preceq \mid\mid \tilde{e} \mid\mid_K \mid\mid \tilde{\epsilon} \mid\mid_K \ . \tag{3.26}$$

In the following subsection we define two families of self-adaptive goal oriented algorithms: one for h-FE spaces, and a second one for hp-FE spaces.

3.1 A Self-Adaptive Goal-Oriented h-Refinement Algorithm

This adaptive algorithm iterates according to the following steps:

1. Solve the direct and dual problems on a given h grid (with arbitrary distribution of p) and the corresponding globally h refined grid $(h/2)$, to obtain u_h, w_h, $u_{h/2}$, and $w_{h/2}$.

2. For each element K, compute

$$\mid\mid\mid (u_{h/2} - u_h) + (w_{h/2} - w_h) \mid\mid_K^2 - \mid\mid (u_{h/2} - u_h) - (w_{h/2} - w_h) \mid\mid_K^2 \mid \tag{3.27}$$

   as an indicator of the error in the goal.

3. Refine those elements contributing with 66% or more of the maximum element error by performing anisotropic refinements if the error is almost one-dimensional.

Notice that for h-adaptive algorithms, only an error indicator (one number per element) is necessary to decide which elements should be refined. Thus, there is no need to use the *projection based interpolation* operator. On the other hand, for hp-adaptive algorithms the full error function (and not just one number per element) is needed to decide between different h and p refinements. For such hp-algorithms, we employ the projection based interpolation operator.

3.2 A Self-Adaptive Goal-Oriented hp-Refinement Algorithm

In this section, we define two goal-oriented hp self-adaptive algorithms that utilize the main ideas of the fully automatic (energy-norm based) hp-adaptive algorithm presented in [9, 17]. We start by recalling the main objective of the self-adaptive (energy-norm based) hp-refinement strategy, which consists of solving the following maximization problem:

$$\begin{cases} \text{Find an optimal } \tilde{hp}\text{-grid in the following sense:} \\ \tilde{hp} = arg \max\limits_{\widehat{hp}} \sum\limits_{K} \dfrac{\mid u - \Pi_{hp}^{K} u \mid_{1,K}^{2} - \mid u - \Pi_{\widehat{hp}}^{K} u \mid_{1,K}^{2}}{\Delta N} \ , \end{cases} \tag{3.28}$$

where

- $u = u_{\frac{h}{2},\, p+1}$ is the *fine grid* solution,
- $\Delta N > 0$ is the increment in the number of unknowns from grid hp to grid $\widehat{hp}$, and
- $|\cdot|_{1,K}$ is the H^1-seminorm for element K.

Similarly, for goal-oriented hp-adaptivity, we propose the following two algorithms based on estimates (3.25) and (3.26):

$$\begin{cases} \text{Find an optimal } \tilde{hp}\text{-grid in the following sense:} \\ \tilde{hp} = arg \max\limits_{\widehat{hp}} \sum\limits_{K} \dfrac{\mid \mid (u+w) - \Pi_{hp}^{K}(u+w) \mid_{1,K}^{2} - \mid (u-w) - \Pi_{hp}^{K}(u-w) \mid_{1,K}^{2} \mid}{\Delta N} \\ \qquad\qquad - \dfrac{\mid \mid (u+w) - \Pi_{\widehat{hp}}^{K}(u+w) \mid_{1,K}^{2} - \mid (u-w) - \Pi_{\widehat{hp}}^{K}(u-w) \mid_{1,K}^{2} \mid}{\Delta N} \end{cases} \tag{3.29}$$

$$\begin{cases} \text{Find an optimal } \tilde{hp}\text{-grid in the following sense:} \\ \tilde{hp} = arg \max\limits_{\widehat{hp}} \sum\limits_{K} \dfrac{\mid u - \Pi_{hp}^{K} u \mid_{1,K} \cdot \mid w - \Pi_{hp}^{K} w \mid_{1,K}}{\Delta N} \\ \qquad\qquad - \dfrac{\mid u - \Pi_{\widehat{hp}}^{K} u \mid_{1,K} \cdot \mid w - \Pi_{\widehat{hp}}^{K} w \mid_{1,K}}{\Delta N} \ , \end{cases} \tag{3.30}$$

where:

- $u = u_{\frac{h}{2},\, p+1}$ and $w = w_{\frac{h}{2},\, p+1}$ are the *fine grid* solutions corresponding to the direct and dual problems,
- $\Delta N > 0$ is the increment in the number of unknowns from grid hp to grid $\widehat{hp}$, and
- $|\cdot|_{1,K}$ is the H^1-seminorm for element K.

Implementation of both goal-oriented *hp*-adaptive algorithms is based on the optimization procedure used for energy-norm *hp*-adaptivity [17].

Implementation details. In what follows, we discuss the main implementation details needed to extend the fully automatic (energy norm based) *hp*-adaptive algorithm [9] to a fully automatic goal-oriented *hp*-adaptive algorithm.

1. First, the solution w of the dual problem in the fine grid is necessary. This goal can be attained either by using a direct (frontal) solver or an iterative (two-grid) solver (see [15]).
2. Subsequently, we should treat both solutions as satisfying two different partial differential equations (PDE's). In the case of algorithm (3.29), we select functions $u + w$ and $u - w$ as the solutions of the system of two (undefined) PDE's. In the case of algorithm (3.30), u and w will be the corresponding solutions.
3. We proceed to redefine the evaluation of the error. For algorithm (3.29), we replace the H^1-seminorm error evaluation of a two dimensional function $(\mid u_1 - \Pi_{hp} u_1 \mid_1^2 + \mid u_2 - \Pi_{hp} u_2 \mid_1^2)$ by the following quantity: $\mid \mid (u+w) - \Pi_{hp}(u+w) \mid_1^2 - \mid (u-w) - \Pi_{hp}(u-w) \mid_1^2 \mid$. For algorithm (3.30), we replace the H^1-seminorm error evaluation of a two dimensional function by $\mid u - \Pi_{hp} u \mid_1 \cdot \mid w - \Pi_{hp} w \mid_1$.
4. After these small modifications, the energy-norm based adaptive algorithm may now be utilized as a fully automatic goal-oriented *hp*-adaptive algorithm.

Appendix C provides a comparison between different energy-norm and goal-oriented based adaptive *h*- and *hp*-algorithms.

4 Direct Current (DC) Logging Applications

In this section, we introduce two DC problems corresponding to different resistivity borehole logging applications.

4.1 A DC Borehole Resistivity Logging Model Problem

We consider the following geometry, sources, receivers, and materials (illustrated in Fig. 1):

- A domain $\Omega = \mathbb{R}^3$.
- One 10 cm-long (infinitely thin) source electrode located on the axis of symmetry and moving along the z-axis.
- Four 5 cm-long (infinitely thin) receiving electrodes located 50 cm, 100 cm, 150 cm, and 200 cm above the source electrode, on the axis of symmetry.
- Material I:
  1. a cylinder Ω_I of radius 10 cm surrounding the axis of axisymmetry ($\Omega_I = \{(\rho, \phi, z) \ : \ \rho \leq 10 \text{ cm}\}$),
  2. with resistivity R=0.1 $\Omega\cdot$ m.
- Material II:
  1. a subdomain Ω_{II} defined by $\Omega_{II} = \{(\rho, \phi, z) \ : \ \rho > 10 \text{ cm} \ , \ 0 \text{ cm} \leq z \leq 100 \text{ cm}\}$,
  2. with resistivity R=1 $\Omega\cdot$ m.
- Material III:
  1. a subdomain Ω_{III} defined by $\Omega_{III} = \{(\rho, \phi, z) \ : \ \rho > 10 \text{ cm} \ , \ -50 \text{ cm} \leq z < 0 \text{ cm}\}$,
  2. with resistivity R=10000 $\Omega\cdot$ m.
- Material IV:
  1. a subdomain Ω_{IV} defined by $\Omega_{IV} = \{(\rho, \phi, z) \ : \ \rho > 10 \text{ cm} \ , \ z < -50 \text{ cm or } z > 100 \text{ cm}\}$,
  2. with resistivity R=100 $\Omega\cdot$ m.

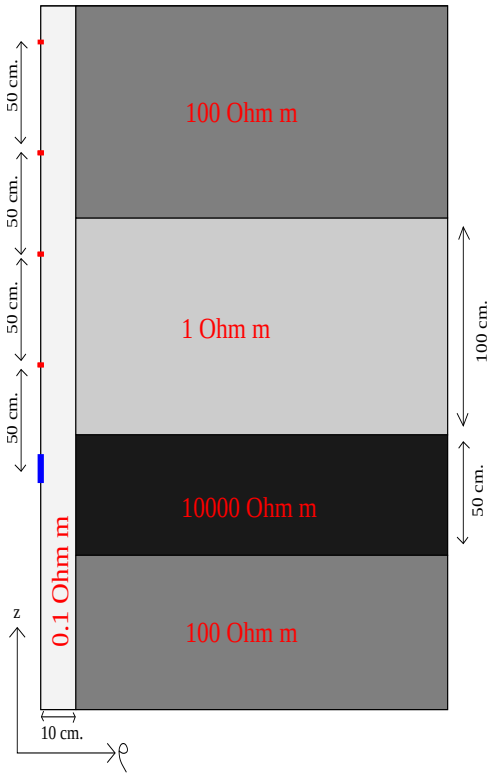

Figure 1: Geometry of the DC resistivity borehole logging model problem. The problem consists of one transmitter and four receiver electrodes, a conductive borehole ($R = 0.1\ \Omega{\cdot}m$), and four layers in the formation material with varying resistivities (from $R = 1\ \Omega \cdot m$ up to $R = 10000\ \Omega \cdot m$).

The source electrode. In this problem, we are interested in modeling a Dirac's delta point source given by $\delta(\rho - 0)\delta(z - z_0)$, where z_0 is a point along the z-axis. A point source modeled with a Dirac's delta will result in a solution with infinite energy, and therefore, it should not be modeled directly with our *hp*-adaptive FE code. Both energy- and goal-driven adaptive mesh optimization algorithms are based on the assumption that the load (also for the dual problem) defines a functional that is continuous in the energy space, with the resulting solutions having finite energy.[2] One possible solution is to "smear" the point source over a finite region,

$$0 < \rho < a\ , \qquad |z - z_0| < \frac{\Delta z}{2}, \tag{4.31}$$

[2]This does not mean that finite elements, in general, cannot be used to model solutions with infinite energy. One possibility is to change the norm in which the convergence is assessed, switching either to fractional Sobolev spaces or Banach spaces $W^{1,p}$ with $p \neq 2$, see [20]. Another possibility is to use the singular component method, see [2]

assuming that the impressed source current $\boldsymbol{J}$ satisfies

$$\boldsymbol{\nabla}\cdot\boldsymbol{J}=\begin{cases}\dfrac{1}{Vol}, & \rho<a,\ |z-z_0|<\frac{\Delta z}{2}\\ 0 & \text{otherwise,}\end{cases} \tag{4.32}$$

where $Vol=\pi a^2\Delta z$ is the volume occupied by the source electrode.

Remark 2. One can always find *a particular* impressed current $\boldsymbol{J}=(J_r,J_\phi,J_z)$ satisfying the condition above, e.g.,

$$J_r=\frac{r}{2Vol},\quad J_\phi=0,\quad J_z=0\,. \tag{4.33}$$

Accordingly, by integrating the source term by parts, we obtain

$$\int_V \boldsymbol{\nabla}\cdot\boldsymbol{J}\,\xi\,dV=-\int_V \boldsymbol{J}\cdot\boldsymbol{\nabla}\xi\,dV+\int_{\partial V}\boldsymbol{n}\cdot\boldsymbol{J}\xi\,dS\,, \tag{4.34}$$

where V is the volume occupied by the antenna. The first integral on the right-hand side of this last equation tends to zero as a tends to zero, *i.e.*,

$$\int_V \boldsymbol{J}\cdot\boldsymbol{\nabla}\xi\,dV=2\pi\int_0^a\int_{-\Delta z/2}^{\Delta z/2}\frac{\rho^2}{2\pi a^2\Delta z}\frac{\partial\xi}{\partial\rho}\,d\rho dz\to 0\,. \tag{4.35}$$

In addition, the boundary integral is independent of parameter a. This is shown as follows:

$$\int_{\partial V}\boldsymbol{n}\cdot\boldsymbol{J}\,\xi\,dS=2\pi\int_{-\Delta z/2}^{\Delta z/2}\frac{a^2}{2\pi a^2\Delta z}\xi\,dz=\frac{1}{\Delta z}\int_{-\Delta z/2}^{\Delta z/2}\xi\,dz\,. \tag{4.36}$$

We discuss the possibility of dropping the first term in the goal-oriented computations in a subsequent section of this paper. ∎

Objective. The objective of the simulation is to determine the electric current I between two receiving electrodes, given by:

$$I=\frac{\Delta V}{R}=\frac{1}{R}\int_a^b\mathbf{E}dl=-\sigma\int_a^b\nabla u dz=-\sigma\int_a^b\frac{\partial u}{\partial z}dz=\sigma(u(a)-u(b))\,, \tag{4.37}$$

where a and b are the locations (in the z-axis) of the two receiving electrodes, and $R=1/\sigma$ is the resistivity. Functional $I:V\longrightarrow\mathbb{R}$ defined by $I(u)=\sigma(u(a)-u(b))$ is not continuous (in the energy norm). We shall replace it by a "regularized functional" obtained using an extraction formula described in Appendix B.

Computational domain. The problem is formulated in $\mathbb{R}^3$. Construction of infinite elements (see [10, 6, 7] for details), or other techniques are unnecessary because the solution decays as $\dfrac{1}{\sigma\, r}$ for $r \to \infty$. We may simply truncate the domain at a large distance, and apply PEC (or Neumann) boundary condition along the truncated boundary.

4.2 Through Casing Resistivity Tool (TCRT) Problem

We consider the following geometry, sources, receivers, and materials (illustrated in Fig. 2).

- A domain $\Omega = \mathbb{R}^3$.
- One 10 cm-long (infinitely thin) source electrode located on the axis of symmetry and moving along the z-axis.
- Three 5 cm-long (infinitely thin) receiving electrodes located 150 cm, 175 cm, and 200 cm above the source electrode, on the axis of symmetry.
- Material I:
  1. a cylinder Ω_I of radius 10 cm surrounding the axis of symmetry ($\Omega_I = \{(\rho, \phi, z) \ : \ \rho \leq 10 \text{ cm}\}$),
  2. with resistivity R=0.1 $\Omega\cdot$ m.
- Material II:
  1. a steel casing Ω_{II} of width 1.27 cm surrounding the borehole ($\Omega_{II} = \{(\rho, \phi, z) \ : \ 10 \text{ cm} \leq \rho \leq 11.27 \text{ cm}\}$),
  2. with resistivity R=0.000001 $\Omega\cdot$ m $= 10^{-6}$ $\Omega\cdot$ m .
- Material III:
  1. a subdomain Ω_{III} defined by $\Omega_{III} = \{(\rho, \phi, z) \ : \ \rho > 11.27 \text{ cm} \ , \ 0 \text{ cm} \leq z \leq 100 \text{ cm}\}$,
  2. with resistivity R=1 $\Omega\cdot$ m.
- Material IV:
  1. a subdomain Ω_{IV} defined by $\Omega_{IV} = \{(\rho, \phi, z) \ : \ \rho > 11.27 \text{ cm} \ , \ -50 \text{ cm} \leq z < 0 \text{ cm}\}$,
  2. with resistivity R=10000 $\Omega\cdot$ m.

- Material V:

  1. a subdomain Ω_V defined by $\Omega_V = \{(\rho, \phi, z) \ : \ \rho > 11.27 \text{ cm} \ , \ z < -50 \text{ cm or } z > 100 \text{ cm}\}$,
  2. with resistivity R=100 $\Omega\cdot$ m.

The source electrode is excited according to formula (4.33) by the impressed surface current $\mathbf{J} = (\frac{r}{2Vol}, 0, 0)$.

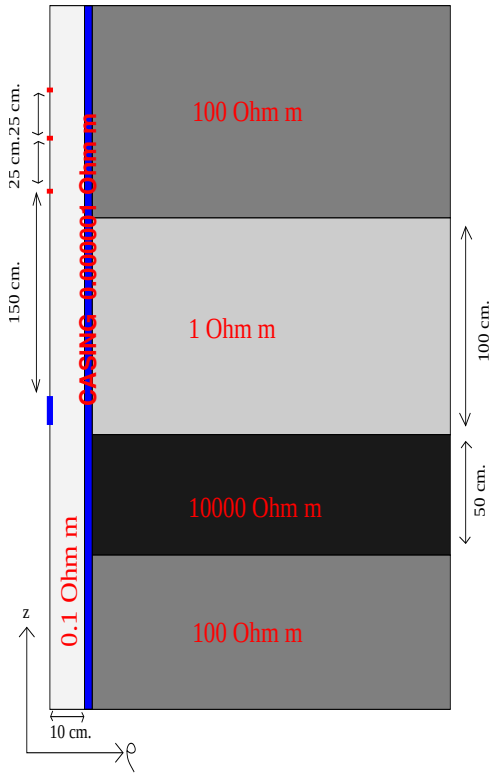

Figure 2: Geometry of a Through Casing Resistivity Tool (TCRT) problem. The model consists of one transmitter and three receiver electrodes, a conductive borehole ($R = 0.1\ \Omega \cdot m$), a metallic casing ($R = 0.000001\ \Omega \cdot m$), and four layers in the formation material with varying resistivities (from $R = 1\ \Omega \cdot m$ to $R = 10000\ \Omega \cdot m$).

Objective. The objective of the simulation is to determine the second difference of the potential $\Delta^2 V$ between the three receiving electrodes, *i.e.*,

$$\Delta^2 V = (u(a_1) - u(a_2)) - (u(a_2) - u(a_3)) \ , \tag{4.38}$$

where a_1, a_2, and a_3 are the locations of the three receiving electrodes.

The functional $\Delta^2 : V \longrightarrow \mathbb{R}$ defined by $\Delta^2(u) = u(a_1) - 2u(a_2) + u(a_3)$ is not continuous and we will again replace it with a post-processing formula (see Appendix B).

5 Numerical Results

In this section, we solve our two Petroleum Engineering applications of interest presented in Section 4 using the self-adaptive *hp* goal-oriented algorithm (3.30).

5.1 A DC Resistivity Logging Model Problem

We first define a stopping criterion for our goal-oriented *hp* self-adaptive strategy. Then, we study numerically the effect that the size of the computational domain has on the quality of the solution. Next, a graph illustrating the exponential convergence of the *hp* goal-oriented self-adaptive strategy (in terms of the problem size vs. quantity of interest I) is displayed along with a number of amplifications of the corresponding final *hp*-grid. Finally, we present the main results describing the final depth profiles of the solution for our DC application.

Stopping criteria. The objective of this simulation is to calculate the electric current I_i between two adjacent receiving electrodes. For a stopping criterion, we will demand that a certain tolerance error TOL in the quantity of interest I_i (on the decibel scale) be met. More precisely, if I_i^{EXACT} represents the electric current corresponding to the exact solution, we want to find I_i^{FE} such that:

$$|10 \log_{10} I_i^{FE} - 10 \log_{10} I_i^{EXACT}| \leq TOL \ . \tag{5.39}$$

Equivalently, we have:

$$10^{-\frac{TOL}{10}} \leq \frac{I_i^{FE}}{I_i^{EXACT}} \leq 10^{\frac{TOL}{10}} \ . \tag{5.40}$$

By subtracting the unity from the above inequality, we obtain the following result:

$$10^{-\frac{TOL}{10}} - 1 \leq \frac{I_i^{FE} - I_i^{EXACT}}{I_i^{EXACT}} \leq 10^{\frac{TOL}{10}} - 1 \ . \tag{5.41}$$

The above condition will be satisfied if the relative error on the quantity of interest is such that:

$$\frac{|I_i^{FE} - I_i^{EXACT}|}{|I_i^{EXACT}|} \leq \max\{10^{\frac{TOL}{10}} - 1 \ , \ 1 - 10^{-\frac{TOL}{10}}\} \ . \tag{5.42}$$

Table 1 shows the relation between the relative error of I in percent, and the absolute error of I in the decibel scale.

Absolute Error (Decibel Scale)	Relative Error (in %)
10^{-6} dB	$2.30 * 10^{-5}$ %
10^{-5} dB	$2.30 * 10^{-4}$ %
10^{-4} dB	$2.30 * 10^{-3}$ %
0.001 dB	0.02303 %
0.01 dB	0.23053 %
0.1 dB	2.32930 %
1 dB	25.8925 %
10 dB	900.000 %

Table 1: Relation between absolute errors (in the decibel scale) and relative errors (in percent), according to formula (5.42).

Size of source electrode and computational domain. The size of the source electrode is dictated by the geometry of the logging tool, in our case, 10 cm.

In order to study the effect of the size of the computational domain on the quality of the solution, Fig. 3 displays the relative error in percent of the quantity of interest I with respect to the distance (in meters) from the receiving electrodes (located at 150 and 200 cm. above the source electrode) to the closest boundary. By selecting this distance as 100 m, we guarantee a relative error on I below 0.1%.

Goal-oriented adaptivity achieves exponential convergence rates. As mentioned in previous sections, the self-adaptive *hp* goal-oriented strategy produces a sequence of grids that converges exponentially in terms of the problem size (number of unknowns of the linear system of equations) vs. the relative error in the quantity of interest (in our case, the electric current I). In order to illustrate the importance of this theoretical result via numerical experimentation, we consider our DC logging problem with the source electrode located at $z = -1$ m, and two receiving electrodes located at $z = 0$ and $z = 0.5$ m, respectively. In Fig. 4, we display the convergence history of $|L(e)| = |\Psi_{h/2,p+1} - \Psi_{h,p}|$ (blue curve), and the more stable upper bound estimate of $|L(e)|$ given by equation (3.26) (red curve). Notice that with less than 15,000 unknowns, we obtain a relative error of I below 0.00001%, *i.e.,* a discretization error below 10^{-6} dB.

In Figures 5, 6, and 7 we display amplifications of the corresponding final *hp*-grid in the vicinity of three of the singularities of the problem. Notice the very strong singularity

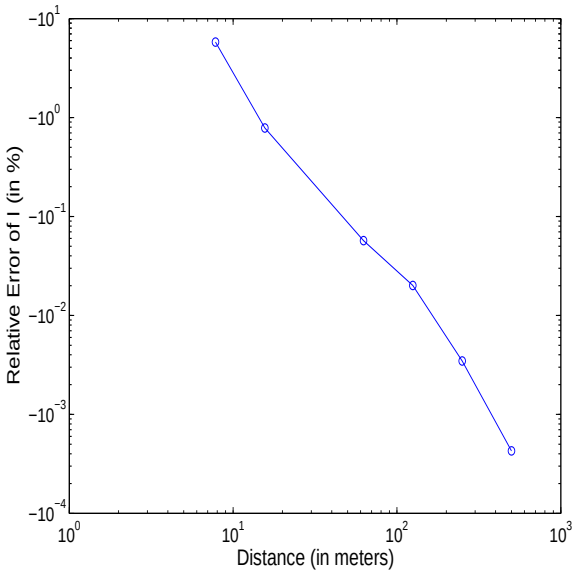

Figure 3: Borehole DC resistivity logging model problem. Size of computational domain (in meters) vs. the relative error (in percent) of the quantity of interest I.

located at point ($\rho = 0.1\ m, z = 0\ m$) (Fig. 5), where three different materials with highly varying conductive properties meet.

Final Logs. At this point, we describe the main result of our computations for the borehole DC resistivity logging model problem, *i.e.*, the electric current on the receiving electrodes as we move the logging instrument along the vertical direction (z-axis). This result is displayed in Fig. 8 (left), where the horizontal axis corresponds to the electric current in the decibel scale, while the vertical axis corresponds to the vertical position (measured every 3 cm) of the receiving electrode. Curves with different colors correspond to different quantities of interest: light blue, dark blue, and black indicate the electric current between the first and second (I_{12}), second and third (I_{23}), and third and fourth (I_{34}) receiving electrodes, respectively. In Fig. 8 (right), we display second differences of the potential, *i.e.* $(I_{12} - I_{23})/\sigma$ (red) and $(I_{23} - I_{34})/\sigma$ (magenta), respectively.

5.2 Through Casing Resistivity Tool (TCRT) Problem

In order to solve numerically the TCRT problem described in Section 4.2, it is necessary to overcome the following challenges:

1. To model materials with varying coefficients of up to ten orders of magnitude (10^{10}).

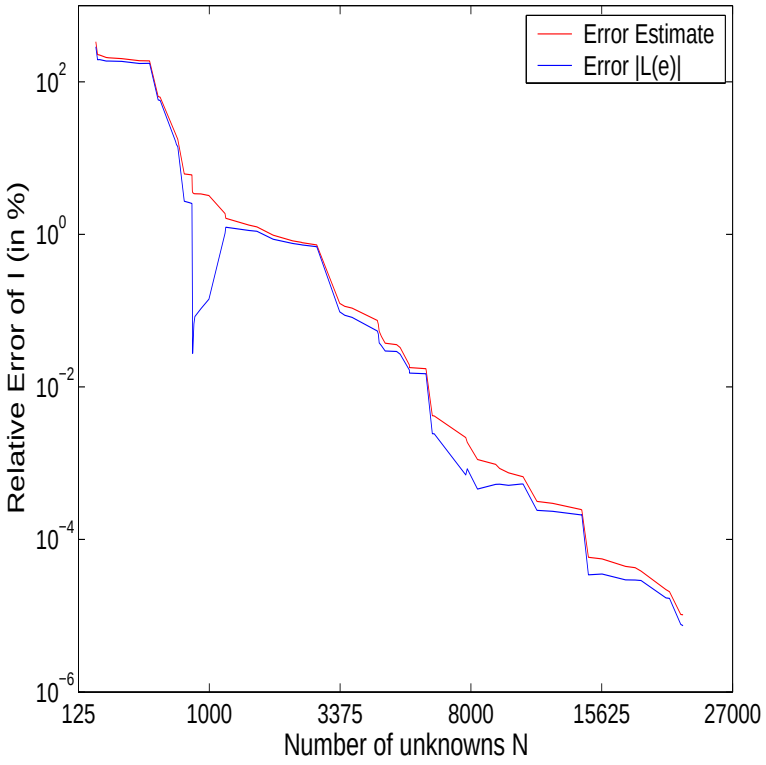

Figure 4: Borehole DC resistivity logging model problem. Convergence history using goal-oriented *hp*-adaptivity. Number of unknowns vs. the relative error (in percent) of the quantity of interest I.

2. To solve the problem in a large computational domain. Due to the presence of steel casing, a large modeling error may be introduced if we consider a domain that is not large enough. Our numerical results indicate the need of a computational domain of size larger than three miles in the vertical direction (if an error below 1% is desired).

3. To calculate second-order differences of the potential at the receiving electrodes. This quantity of interest is up to nine orders of magnitude smaller than the solution itself. In this context, energy-norm based adaptive techniques are inappropriate, and goal-oriented adaptivity becomes essential.

In the remainder of this section, we describe our stopping criterion. We also compare our numerical solution vs. the analytical solution presented in Section A for a formation composed by a single homogeneous material, and we present the final log corresponding to our TCRT problem.

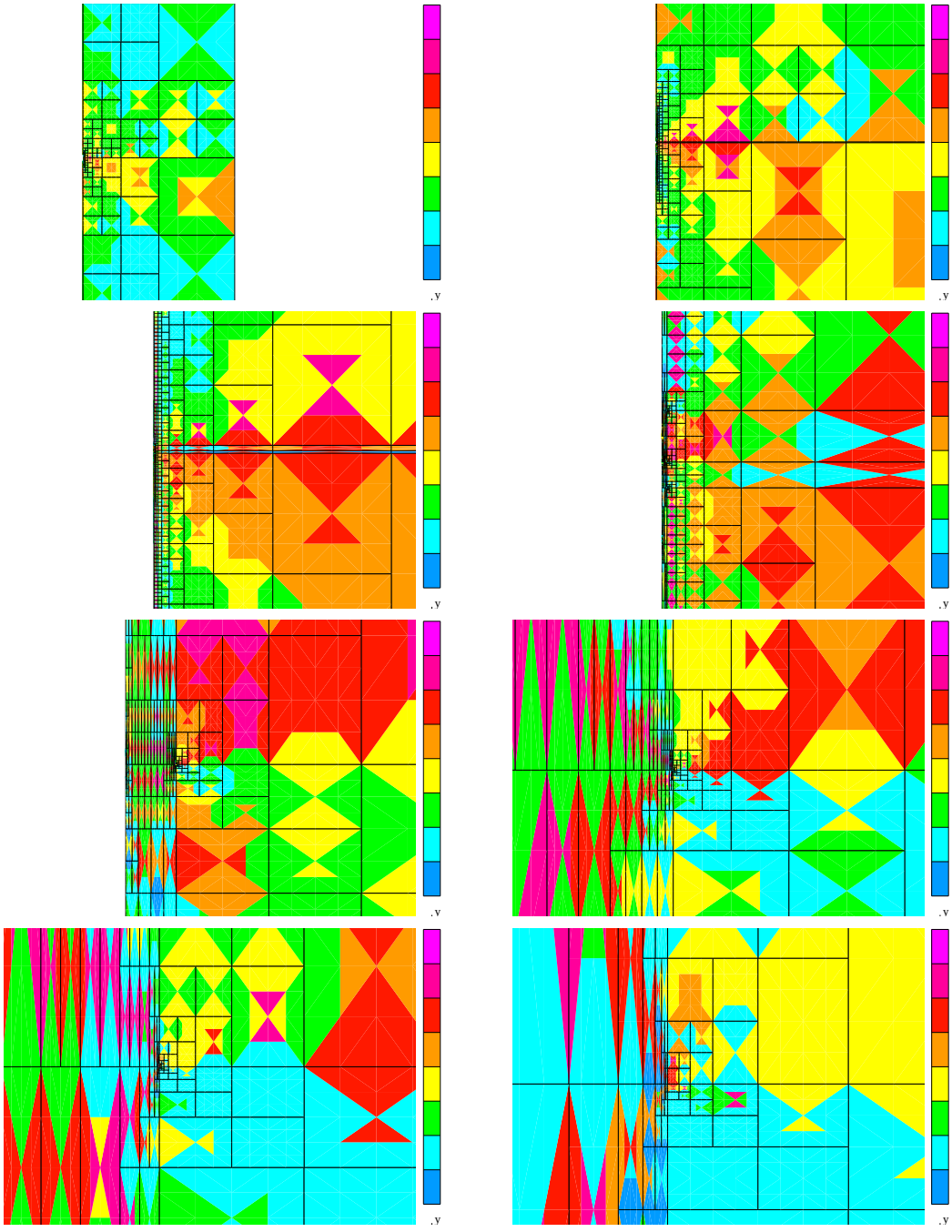

Figure 5: Final *hp*-grid for the borehole DC resistivity logging model problem. Progressive amplifications by factors of 1 (1st row left), 10 (1st row right), 100 (2nd row left), 1000 (2nd row right), 10^4 (3rd row left), 10^5 (3rd row right), 10^6 (bottom row left), and 10^7 (bottom row right) toward a singularity located at ($\rho = 0.1\ m, z = 0\ m$). Different colors indicate different polynomial orders of approximation, ranging from 1 (blue) to 8 (pink).

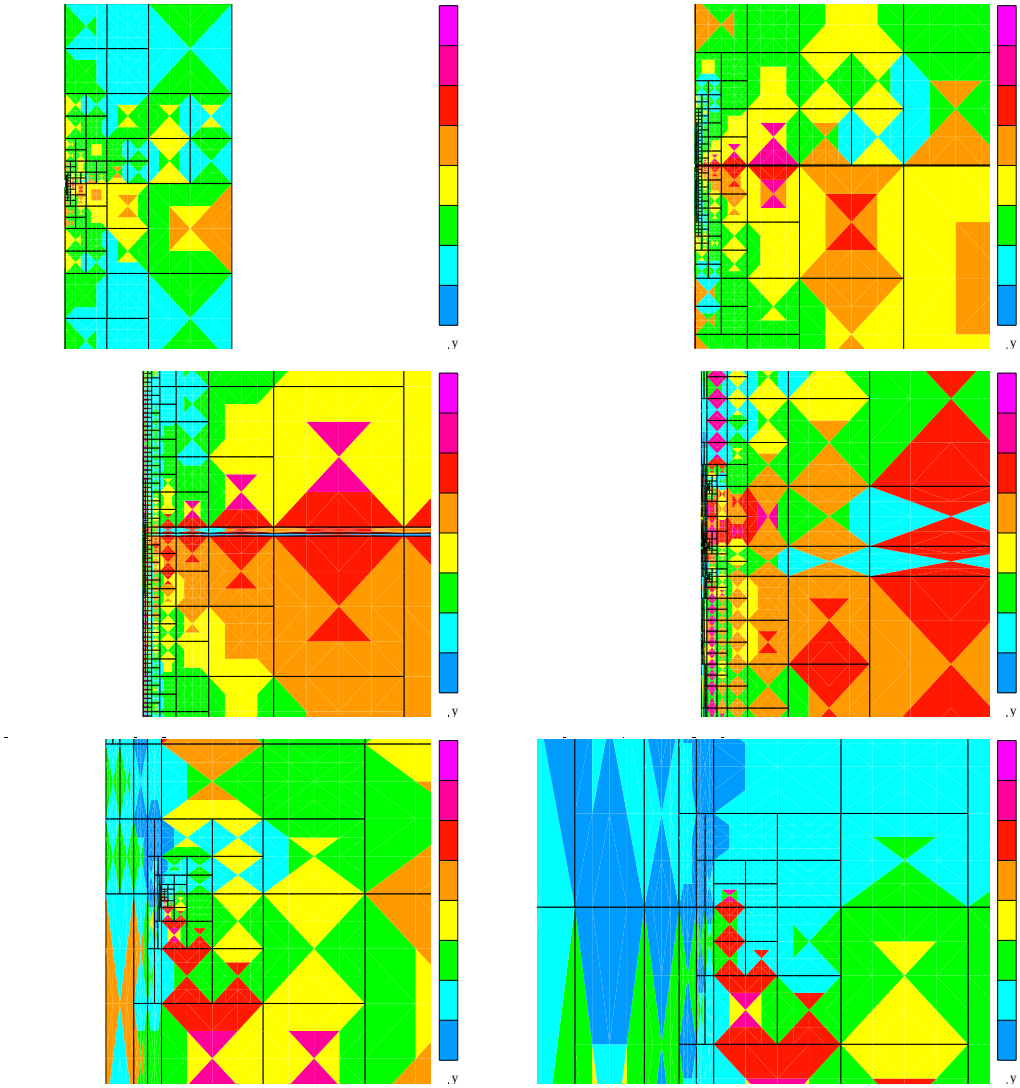

Figure 6: Final *hp*-grid for the borehole DC resistivity logging model problem. Progressive amplifications by factors of 1 (1st row left), 10 (1st row right), 100 (2nd row left), 1000 (2nd row right), 10^4 (bottom row left), and 10^5 (bottom row right) toward a singularity located at ($\rho = 0.1\ m, z = -0.5\ m$). Different colors indicate different polynomial orders of approximation, ranging from 1 (blue) to 8 (pink).

Stopping criteria. For our stopping criterion, we will demand that the relative error in the quantity of interest (second difference of potential) be below 0.25%.

Agreement between numerical and analytical solutions . We compare two approximate solutions for the TCRT problem:

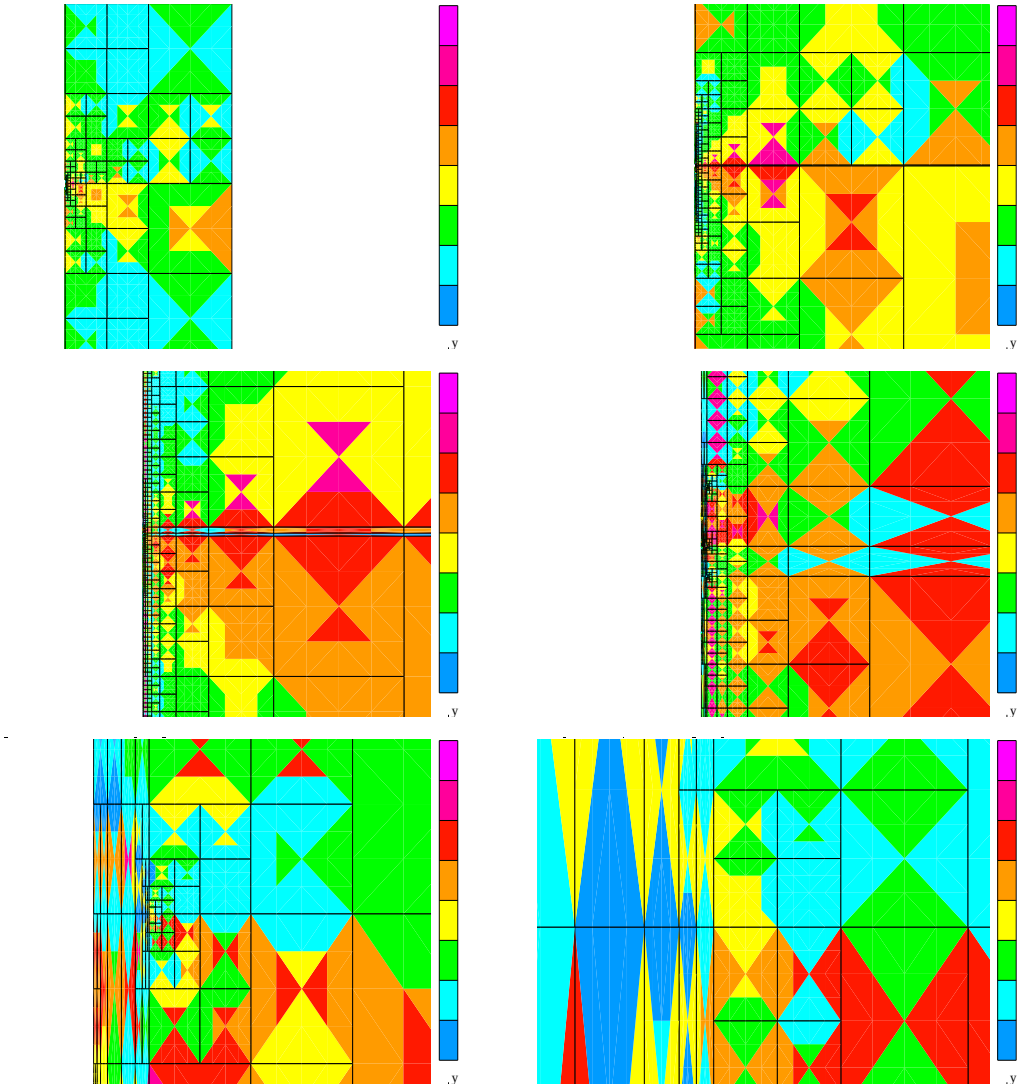

Figure 7: Final *hp*-grid for the borehole DC resistivity logging model problem. Progressive amplifications by factors of 1 (1st row left), 10 (1st row right), 100 (2nd row left), 1000 (2nd row right), 10^4 (bottom row left), and 10^5 (bottom row right) toward a singularity located at ($\rho = 0.1\ m, z = 1\ m$). Different colors indicate different polynomial orders of approximation, ranging from 1 (blue) to 8 (pink).

1. Solution u^{FEM}, obtained using the fully automatic goal-oriented hp-FE algorithm, and
2. Solution $u^{ANALYTICAL}$, obtained by evaluating numerically the analytical solution described in Appendix A.

For the solution u^{FEM}, we estimated the discretization error by comparing the solution of the problem in a given *hp*-grid against the corresponding globally refined grid, *i.e.*, in the

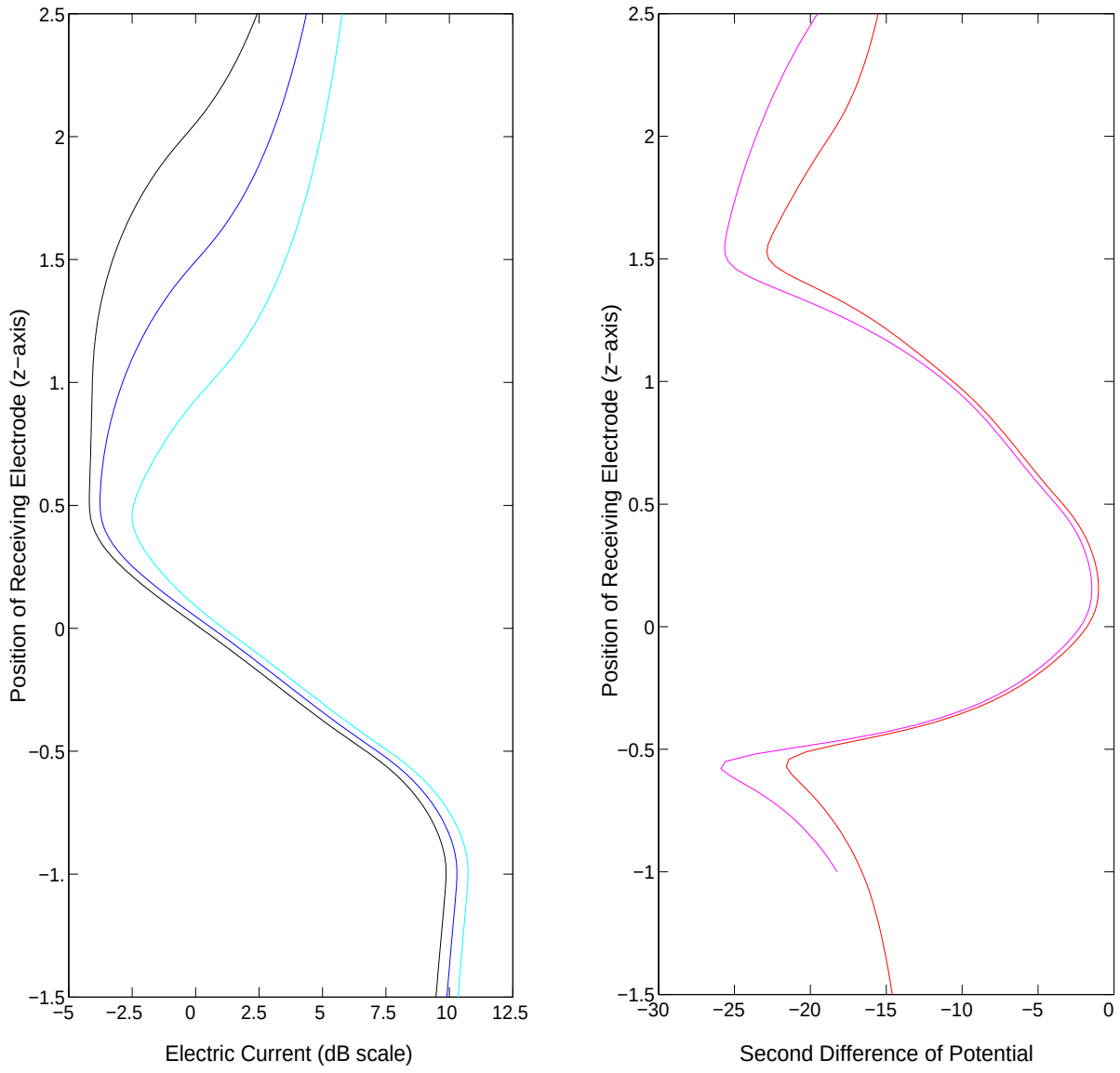

Figure 8: DC resistivity logging model problem. Left-hand panel: Electric current (Amperes in decibel scale) vs. position in the z-axis of the first receiving electrode (in meters). Right-hand panel: Second difference of potential (Volts in decibel scale) vs. position in the z-axis of the second receiving electrode (in meters). Curves with different colors describe the measurement of electric current or second difference of potential for different receiving electrodes.

grid $h/2, p+1$. Using this reliable error estimate, we obtained a relative error in the second difference of the potential below 0.01%.

$u^{ANALYTICAL}$ was computed numerically using a special evaluation of premultiplied Bessel functions (using D.E. Amos' libraries [1]), and adaptive integration based on Folin and Simpson's rules. Due to round-off errors, we were not able to guarantee a relative error below 1% in most cases. Notice that $10-13$ digits of the exact solution may be needed in order to guarantee a relative error in the second difference of the potential below 1%.

From this discussion it follows that, paradoxically, our FE solution is more reliable than the numerical evaluation of the analytical solution. Comparative results are displayed in Table 2.

Casing Resistivity: $10^{-6}\ \Omega \cdot m.$			
Formation Resistivity	$1\ \Omega \cdot m.$	$10\ \Omega \cdot m.$	$100\ \Omega \cdot m.$
u^{FEM}	-73.89228	-79.2206	-84.4104
$u^{ANALYTICAL}$	-73.89233	-79.2173	-84.5906

Casing Resistivity: $10^{-7}\ \Omega \cdot m.$		
Formation Resistivity	$1\ \Omega \cdot m.$	$10\ \Omega \cdot m.$
u^{FEM}	-89.21715	-94.5940
$u^{ANALYTICAL}$	-89.24749	-105.0936

Table 2: TCRT problem. Second difference of the potential (Volts in decibel scale) for two solutions, one obtained using the FEM, and the other obtained with the numerical evaluation of the analytical solution.

Final log. At this point, we present the main result of our computations for the TCRT problem, *i.e.*, the second difference of the potential on the receiving electrodes as we move the logging instrument in the z direction. This result is displayed in Fig. 9 (left), where the horizontal axis corresponds to the second difference of the potential in Volts in the decibel scale. The vertical axis indicates the vertical position (measured every 3 cm) of the second receiving electrode. If we consider a casing of resistivity $10^{-7}\ \Omega \cdot m$ (as opposed to $10^{-6}\ \Omega \cdot m$), similar results are obtained, with the exception that the scales will be shifted by approximately 16.6 dB, see Fig. 9 (right).

Finally, in Fig. 10 we display the error and number of unknowns of the associated system of linear equations vs. position in the z-axis of the second receiving electrode. With fewer than 9000 unknowns, we guarantee a relative error in the second difference of potential below 0.25 %. Notice that the number of unknowns grows with respect to the position of the receiving electrode. This is because as we moved the logging instrument (from bottom to top) we employed the grid from the previous position as our starting point.

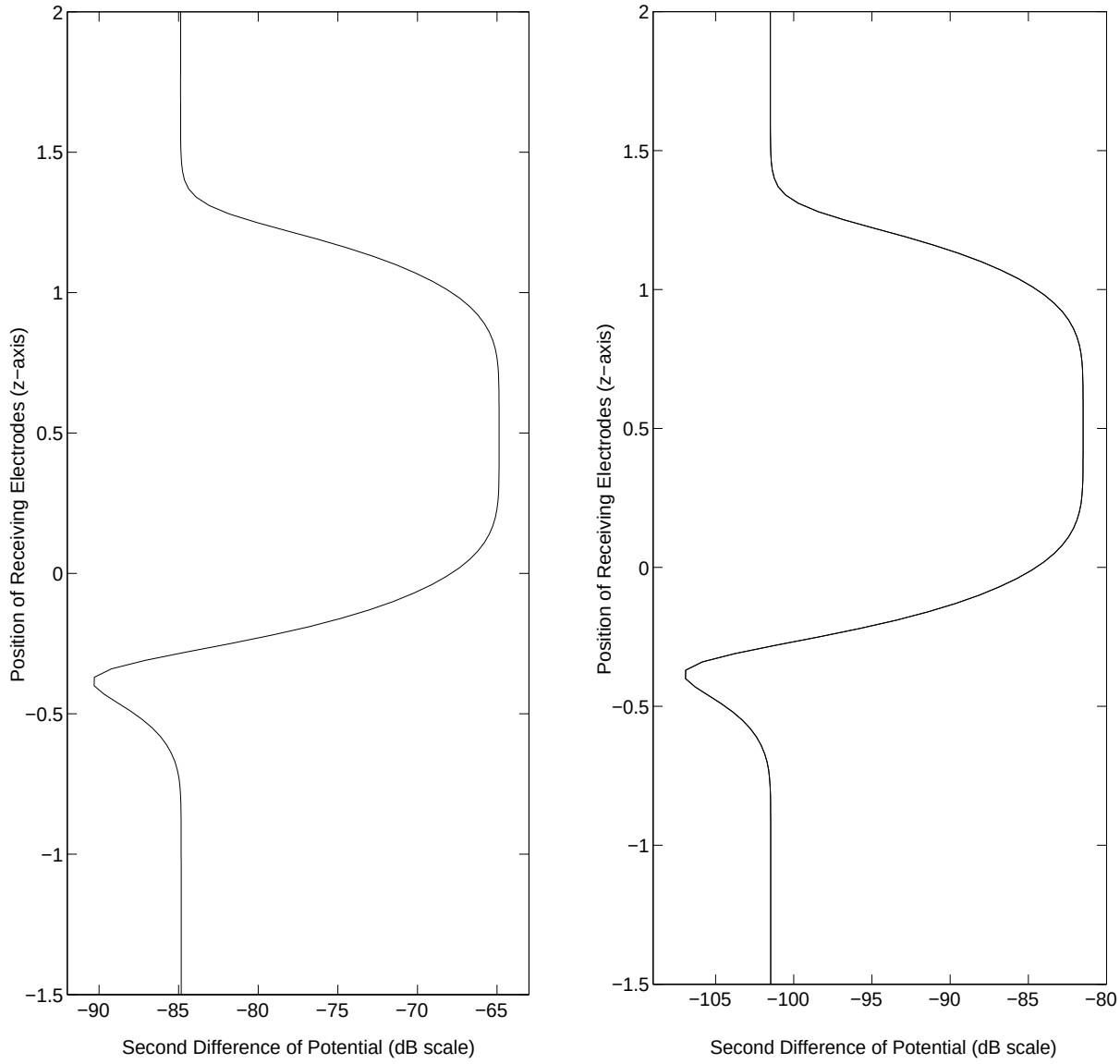

Figure 9: TCRT problem. Second differences of the potential (Volts in decibel scale) vs. position in the z-axis of the second receiving electrode (in meters). Resistivity of the casing is equal to $10^{-6}\ \Omega \cdot m$ (left panel) and $10^{-7}\ \Omega \cdot m$ (right panel), respectively

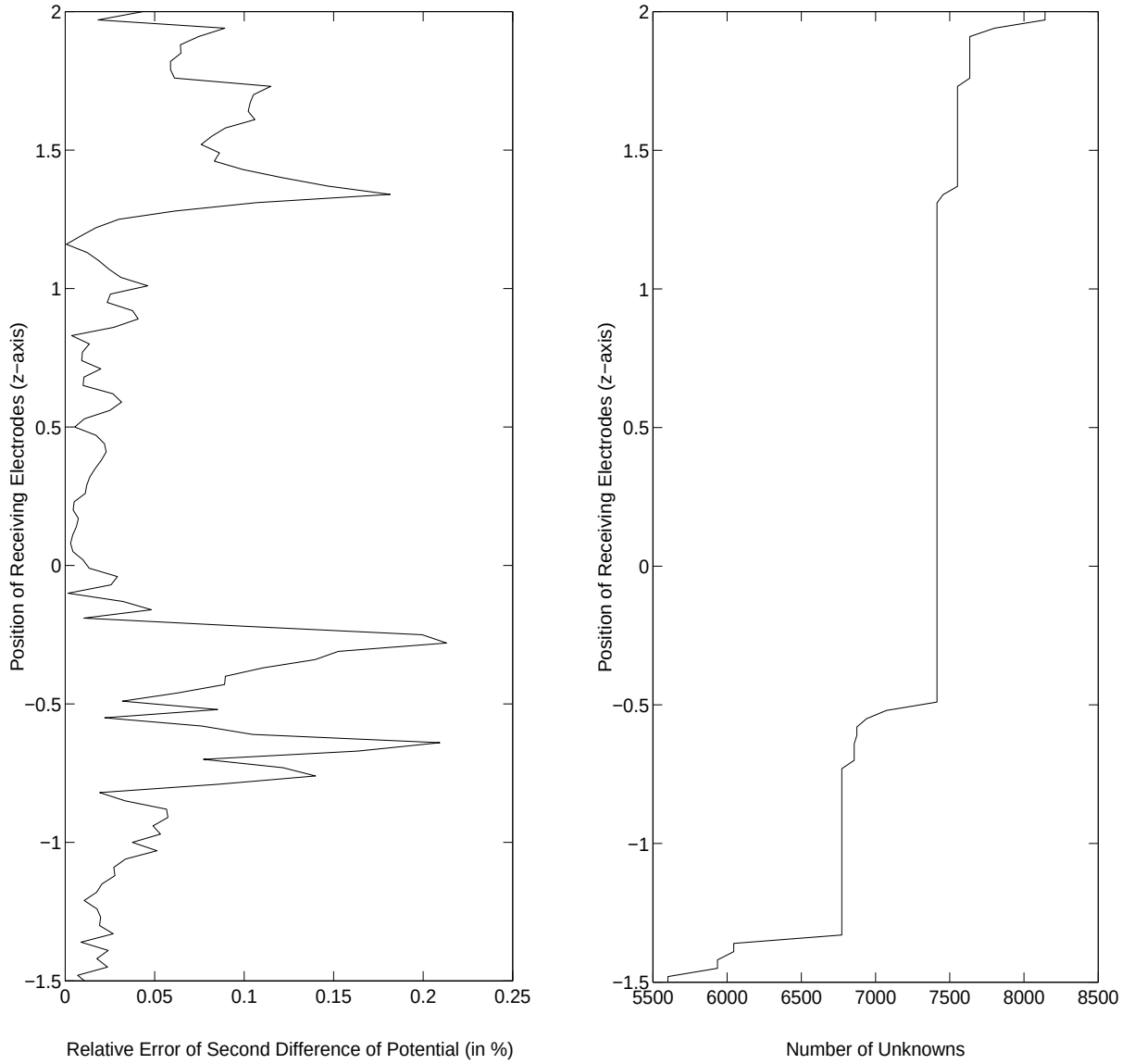

Figure 10: TCRT problem. Error (left panel) of second differences of potential (in percentage) and number of unknowns of the corresponding linear system of equations (right panel) vs. position in the z-axis of the receiving electrode (in meters).

6 Conclusions and Future Work

In this paper, we have designed, implemented, and studied both theoretically and numerically a family of goal-oriented self-adaptive algorithms. These algorithms produce automatically (without any user interaction) a sequence of optimal h or hp-grids, intended to minimize the error of a prescribed quantity of interest with respect to the problem size. Comparative nu-

merical results illustrate the superior convergence of self-adaptive goal-oriented *hp*-adaptive algorithms with respect to both goal-oriented *h*-adaptivity, and energy-norm based *h*- and *hp*-adaptivity (see Appendix C).

The goal-oriented *hp*-adaptive algorithm combines goal-oriented adaptivity (thus, a particular feature of the solution is pursued) with *hp*-Finite Elements (delivering exponential convergence rates). Numerical results showed that the exponential convergence of the method is as predicted by the theory.

We also applied the fully automatic goal-oriented *hp*-adaptive strategy to simulate two Petroleum Engineering applications: a DC resistivity logging instrument in a borehole environment, and a Trough Casing Resistivity Tool (TCRT). The self-adaptive goal-oriented *hp*-FE strategy allowed for extremely accurate simulations of the response of our two logging applications of interest. Indeed, the method delivers a solution with a discretization error that is several orders of magnitude below the sensitivity threshold of the actual receiving electrodes.

A generalization of these algorithms to Helmholtz and Maxwell's equations will be formulated and implemented in a forthcoming paper. For electrodynamic simulations of borehole logging instruments, the use of essential. Electromagnetic fields decay exponentially as we move away from the source antenna(s) (and thus, energy-norm based adaptivity becomes inappropriate), and there is an increasing need for the use of goal-oriented adaptive algorithms to accurately simulate the response of borehole logging instruments.

Acknowledgment

This work has been financially supported by Baker-Atlas. We would also like to acknowledge the expertise and technical advise received from A. Bespalov, T. Wang, and other members of the Science Department of Baker-Atlas.

References

[1] D.E. Amos. A portable package for Bessel functions of a complex argument and non-negative order. *ACM Trans. Math. Softw.*, 12:265–273, 1986.

[2] F. Assous, C.(Jr.) Ciarlet, S. Labrunie, and S. Lohrengel. The singular complement method. In *13th Intl Conf. on Domain Decomposition Methods, CIMNE, Barcelona, p. 161-189.* N. Debit et al., 2002.

[3] I. Babuska and A. Miller. The post-processing approach in the finite element method. I. Calculation of displacements, stresses and other higher derivatives of the displacements. *Int. J. Numer. Methods Eng.*, 20:1085–1109, 1984.

[4] I. Babuska and A. Miller. The post-processing approach in the finite element method. II. The calculation of stress intensity factors. *Int. J. Numer. Methods Eng.*, 20:1111–1129, 1984.

[5] R. Becker and R. Rannacher. Weighted a posteriori error control in FE methods. In *ENUMATH 97. Proceedings of the 2nd European conference on numerical mathematics and advanced applications held in Heidelberg, Germany, September 28-October 3, 1997. Including a selection of papers from the 1st conference (ENUMATH 95) held in Paris, France, September 1995. Singapore: World Scientific. 621-637* . Bock, Hans Georg (ed.) et al., 1998.

[6] W. Cecot, L. Demkowicz, and W. Rachowicz. A two-dimensional infinite element for Maxwell's equations. *Comput. Methods Appl. Mech. Eng.*, 188(1-3):625–643, 2000.

[7] W. Cecot, W. Rachowicz, and L. Demkowicz. An *hp*-adaptive finite element method for electromagnetics. III: A three-dimensional infinite element for Maxwell's equations. *Int. J. Numer. Methods Eng.*, 57(7):899–921, 2003.

[8] L. Demkowicz and A. Buffa. H^1, $H(\mathbf{curl})$, and $H(div)$ conforming projection-based interpolation in three dimensions: quasi optimal p-interpolation estimates. Technical Report 04, ICES Report, 2004.

[9] L. Demkowicz, W. Rachowicz, and Ph. Devloo. A fully automatic *hp*-adaptivity. *J. Sci. Comput.*, 17(1-4):117–142, 2002.

[10] K. Gerdes and L. Demkowicz. Solution of 3D-Laplace and Helmholtz equations in exterior domains using *hp*-infinite elements. *Comput. Methods Appl. Mech. Eng.*, 137(3-4):239–273, 1996.

[11] V. Heuveline and R. Rannacher. Duality-based adaptivity in the *hp*-finite element method. *J. Numer. Math.*, 11(2):95–113, 2003.

[12] A. A. Kaufman. The electrical field in a borehole with casing. *Geophysics*, 55(1):29–38, 1990.

[13] J.T. Oden and S. Prudhomme. Goal-oriented error estimation and adaptivity for the finite element method. *Comput. Math. Appl.*, 41(5-6):735–756, 2001.

[14] M. Paraschivoiu and A. T. Patera. A hierarchical duality approach to bounds for the outputs of partial differential equations. *Comput. Methods Appl. Mech. Eng.*, 158(3-4):389–407, 1998.

[15] D. Pardo. *Integration of hp-adaptivity with a two grid solver: applications to electromagnetics.* PhD thesis, The University of Texas at Austin, April 2004.

[16] S. Prudhomme and J.T. Oden. On goal-oriented error estimation for elliptic problems: application to the control of pointwise errors. *Comput. Methods Appl. Mech. Eng.*, 176(1-4):313–331, 1999.

[17] W. Rachowicz, D. Pardo, and L. Demkowicz. Fully automatic *hp*-adaptivity in three dimensions. Technical Report 04-22, ICES Report, 2004.

[18] R. Rannacher and F.T. Suttmeier. A posteriori error control in finite element methods via duality techniques: application to perfect plasticity. *Comput. Mech.*, 21(2):123–133, 1998.

[19] C. J. Schenkel and H. F. Morrison. Electrical resistivity measurement through metal casing. *Geophysics*, 59(7):1072–1082, 1994.

[20] R. Scott. The finite element method with singular data. *Numer. Math.*, 21:317–327, 1973.

[21] P. Solin and L. Demkowicz. Goal-oriented *hp*-adaptivity for elliptic problems. *Comput. Methods Appl. Mech. Eng.*, 193(6-8):449–468, 2004.

[22] D. Xue and L. Demkowicz. Reconstructing of G^1 surfaces with biquartic patches and other techniques. Technical Report 03-51, ICES Report, 2003.

A Analytical solutions.

For testing purposes, we derive analytical solutions to two model problems.

A.1 Radiation from a Point Source embedded in a Homogeneous Medium.

We wish to solve the partial differential equation (in cylindrical coordinates)

$$-\frac{1}{\rho}\frac{\partial}{\partial\rho}(\sigma\rho\frac{\partial u}{\partial\rho}) - \sigma\frac{\partial^2 u}{\partial z^2} = \delta(\rho-\rho_0)\delta(z)\ , \tag{A.43}$$

with the decay condition

$$u(\rho,z)\to 0\ , \quad \text{as } \rho,z\to\infty\ , \tag{A.44}$$

and an additional condition resulting from the axisymmetry assumption; *i.e.*,

$$\frac{\partial u}{\partial r}(0,z) = 0\ . \tag{A.45}$$

The solution can be obtained using the superposition principle, by integrating the fundamental solution:

$$u(\mathbf{x}) = \frac{1}{4\pi\sigma}\int_c \frac{1}{|\mathbf{x}-\mathbf{x_0}|}ds\ , \tag{A.46}$$

where c denotes the circular source. In anticipation of the next problem, we shall use a solution technique based on the Fourier transform and Bessel functions.

By taking the Fourier transform in z, we obtain

$$-\sigma(\frac{1}{\rho}\frac{\partial}{\partial\rho}\rho\frac{\partial\tilde{u}}{\partial\rho}) + \sigma k_z^2\tilde{u} = \delta(\rho-\rho_0)\ , \tag{A.47}$$

where $\tilde{u}$ is the Fourier transform of u. The solution of (A.47) consists of two branches

$$\tilde{u}(\rho) = \begin{cases} \tilde{u}_1(\rho) & 0<\rho<\rho_0 \\ \\ \tilde{u}_2(\rho) & \rho>\rho_0 \end{cases}\ , \tag{A.48}$$

that are solutions of the homogeneous Ordinary Differential Equation (ODE)

$$-\frac{1}{\rho}(\tilde{u}' + \rho\tilde{u}'') + k_z^2\tilde{u} = 0\ , \tag{A.49}$$

with the additional interface conditions:

$$\begin{cases} \tilde{u}_1(\rho_0) = \tilde{u}_2(\rho_0) \\ \tilde{u}_1'(\rho_0) - \tilde{u}_2'(\rho_0) = \dfrac{1}{2\pi\rho_0\sigma} \end{cases} . \tag{A.50}$$

Multiplying (A.49) by ρ^2, and using the change of variables $x = \rho \cdot k_z$, we obtain the modified Bessel equation:

$$x^2\tilde{u}'' + x\tilde{u}' - x^2\tilde{u} = 0 \, . \tag{A.51}$$

The corresponding space of solutions is given by the span of any two linearly independent solutions of (A.51). For example:

$$\tilde{u}(x) = C_1 I_0(x) + C_2 K_0(x) \, , \tag{A.52}$$

where C_1 and C_2 are constants to be determined, I_0 and K_0 are the so called *Bessel functions of imaginary argument*, also referred to as the *modified Bessel Functions*.

Consequently,

$$\tilde{u}_1(\rho, k_z) = C_1 I_0(k_z\rho) + C_2 K_0(k_z\rho) \, , \text{ and} \tag{A.53}$$

$$\tilde{u}_2(\rho, k_z) = C_3 I_0(k_z\rho) + C_4 K_0(k_z\rho) \, . \tag{A.54}$$

If $k_z > 0$ (thus $k_z\rho > 0$) condition (A.45) implies $C_2 = 0$, and condition (A.44) implies $C_3 = 0$. If $k_z < 0$ conditions (A.45), and (A.44) imply a non-trivial combination of complex valued constants C_i , $i = 1...4$. This indicates that the choice of the two linearly independent solutions made in (A.52) is inadequate to represent the solution when $k_z < 0$ (in the sense that algebraic derivations as well as computations become both rather challenging and tedious). Furthermore, K_0 is not symmetric ($K_0(x) \neq K_0(-x)$), and by using the representation (A.53)-(A.54) we lose the symmetry properties of $\tilde{u}(k_z)$. Therefore, we select the following new representation for our solution:

$$\tilde{u}(\rho, k_z) = C_1 I_0(|k_z|\rho) + C_2 K_0(|k_z|\rho) \, . \tag{A.55}$$

Accordingly, in terms of $\tilde{u}_1$ and $\tilde{u}_2$, we have:

$$\tilde{u}_1(\rho, k_z) = C_1 I_0(|k_z|\rho) + C_2 K_0(|k_z|\rho) \, , \text{ and} \tag{A.56}$$

$$\tilde{u}_2(\rho, k_z) = C_3 I_0(|k_z|\rho) + C_4 K_0(|k_z|\rho) \, . \tag{A.57}$$

Now, for every k_z condition (A.45) implies $C_2 = 0$, and condition (A.44) implies $C_3 = 0$. Finally, condition (A.50) implies:

$$C_1 I_0(|k_z|\rho_0) = C_4 K_0(|k_z|\rho_0) \ , \text{ and} \tag{A.58}$$

$$k_z[C_1 I_1(|k_z|\rho_0) + C_4 K_1(|k_z|\rho_0)] = \frac{1}{\sqrt{2\pi}} \frac{1}{2\pi\rho_0\sigma} \ . \tag{A.59}$$

To derive the last equation, we have used the identities:

$$I_0'(|k_z|\rho_0) = |k_z| I_1(|k_z|\rho_0) \ , \tag{A.60}$$

$$K_0'(|k_z|\rho_0) = -|k_z| K_1(|k_z|\rho_0) \text{ , and } \tilde{u}_1'(\rho_0) - \tilde{u}_2'(\rho_0) = \frac{1}{\sqrt{2\pi}} \frac{1}{2\pi\rho_0\sigma} \ . \tag{A.61}$$

By solving the linear system of two equations given by (A.58), and (A.59) we obtain

$$C_4 = \frac{1}{\sqrt{2\pi}} \frac{1}{2\pi\sigma\rho_0|k_z|} \frac{I_0(|k_z|\rho_0)}{K_0(|k_z|\rho_0) I_1(|k_z|\rho_0) + K_1(|k_z|\rho_0) I_0(|k_z|\rho_0)} \ , \text{ and} \tag{A.62}$$

$$C_1 = C_4 \frac{K_0(|k_z|\rho_0)}{I_0(|k_z|\rho_0)} \ . \tag{A.63}$$

Using the Wronskian relationship ($I_0(x)K_1(x) + I_1(x)K_0(x) = 1/x$), we conclude

$$\tilde{u}_1(\rho, k_z) = \frac{K_0(|k_z|\rho_0)}{(2\pi)^{3/2}\sigma} I_0(|k_z|\rho) \text{ , and} \tag{A.64}$$

$$\tilde{u}_2(\rho, k_z) = \frac{I_0(|k_z|\rho_0)}{(2\pi)^{3/2}\sigma} K_0(|k_z|\rho) \ . \tag{A.65}$$

Application of the inverse Fourier transform yields the final solution, namely,

$$u(\rho, z) = \begin{cases} u_1(\rho, z) = \dfrac{1}{\sqrt{2\pi}} \displaystyle\int_{-\infty}^{\infty} \tilde{u}_1(\rho, k_z) \exp^{jk_z \cdot z} \, dk_z & 0 < \rho < \rho_0 \\ u_2(\rho, z) = \dfrac{1}{\sqrt{2\pi}} \displaystyle\int_{-\infty}^{\infty} \tilde{u}_2(\rho, k_z) \exp^{jk_z \cdot z} \, dk_z & \rho > \rho_0 \end{cases} \ . \tag{A.66}$$

Remark 3. By taking the limit $\rho_0 \to 0$, we can recover the solution corresponding to the point source. Branch $\tilde{u}_1$ disappears, and $\tilde{u}_2 = \tilde{u}$ becomes:

$$\tilde{u} = \tilde{u}_2(\rho, k_z) = \frac{1}{(2\pi)^{3/2}\sigma} K_0(|k_z|\rho) \ . \tag{A.67}$$

Thus,

$$u(\rho) = \int_{-\infty}^{\infty} \frac{K_0(|k_z|\rho)}{4\pi^2\sigma} \exp^{jk_z z} \, dk_z \ = \frac{2}{4\pi^2\sigma} \int_0^{\infty} K_0(k_z\rho) \cos(k_z z) dk_z \ = \frac{1}{4\pi\sigma R} \ , \tag{A.68}$$

where $R = \dfrac{1}{\sqrt{\rho^2 + z^2}}$. In the last line, we have used the following two observations:

- The absolute value is a symmetric function (and thus $K_0(|k_z|\rho) = K_0(|-k_z|\rho)$).
- For any symmetric function $f(x)$, we have:

$$\int_{-\infty}^{\infty} f(x)\exp^{jxz}\,dx \;= \int_0^{\infty} f(-x)\exp^{-jxz}\,dx \;+ \int_0^{\infty} f(x)\exp^{jxz}\,dx \;= \tag{A.69}$$

$$2\int_0^{\infty} f(x)\cos(xz)dx\;. \tag{A.70}$$

∎

Remark 4. For a source electrode of finite size, $2L$, the corresponding interface condition becomes $\tilde{u}_1'(\rho_0) - \tilde{u}_2'(\rho_0) = \dfrac{2\sin(|k_z|L)}{4L\pi\rho_0\sigma}$, (A.59) becomes $|k_z|[C_1 I_1(|k_z|\rho_0) + C_4 K_1(|k_z|\rho_0)] = \dfrac{1}{\sqrt{2\pi}}\dfrac{2\sin(|k_z|L)}{4L\pi\rho_0\sigma}$, and (A.68) simplifies to:

$$u(\rho,z) = \frac{1}{2\pi^2\sigma}\int_0^{\infty}\frac{\sin(|k_z|L)}{|k_z|L}K_0(|k_z|\rho)\cos(|k_z|z)dk_z\;. \tag{A.71}$$

∎

A.2 Radiation of a Point Source Through Steel Casing.

At this point, we consider a Through Casing Resistivity Tool (TCRT) problem with a single formation material. That is, we have a source point electrode located at $(\rho = 0, z = 0)$ radiating into a region with three different conductivities: σ_1 (for $r \le \rho_1$), σ_2 (for $\rho_1 < \rho \le \rho_2$), and σ_3 (for $\rho_2 < \rho$), respectively. According to (A.55), we may consider:

$$\tilde{u}_1(\rho,k_z) = C_1 I_0(|k_z|\rho) + C_2 K_0(|k_z|\rho)\;, \tag{A.72}$$

$$\tilde{u}_2(\rho,k_z) = C_3 I_0(|k_z|\rho) + C_4 K_0(|k_z|\rho)\;,\ \text{and} \tag{A.73}$$

$$\tilde{u}_3(\rho,k_z) = C_5 I_0(|k_z|\rho) + C_6 K_0(|k_z|\rho)\;. \tag{A.74}$$

The decaying boundary condition at infinity implies $C_5 = 0$. Accordint to eq. (A.67), the source term at $\rho = 0$ translates into the condition:

$$C_2 = \frac{1}{(2\pi)^{3/2}\sigma_1}\;. \tag{A.75}$$

The remaining four interface conditions that are needed to determine C_1, C_3, C_4, and C_6 are:

$$\tilde{u}_1(\rho_1) = \tilde{u}_2(\rho_1) \ , \tag{A.76}$$

$$\tilde{u}_2(\rho_2) = \tilde{u}_3(\rho_2) \ , \tag{A.77}$$

$$\sigma_1 \tilde{u}_1'(\rho_1) = \sigma_2 \tilde{u}_2'(\rho_1) \ , \text{ and} \tag{A.78}$$

$$\sigma_2 \tilde{u}_2'(\rho_2) = \sigma_3 \tilde{u}_3'(\rho_2) \ . \tag{A.79}$$

Equations (A.76) and (A.78) imply:

$$C_1 I_0(|k_z|\rho_1) + C_2 I_0(|k_z|\rho_1) = C_3 I_0(|k_z|\rho_1) + C_4 I_0(|k_z|\rho_1) \ , \text{ and} \tag{A.80}$$

$$C_1 I_1(|k_z|\rho_1) - C_2 I_1(|k_z|\rho_1) = \mu_{21}[C_3 I_0(|k_z|\rho_1) + C_4 I_0(|k_z|\rho_1)] \ , \tag{A.81}$$

where $\mu_{21} = \sigma_2/\sigma_1$. By solving for C_3 and C_4, we obtain:

$$C_3 = [1 - AK_0(|k_z|\rho_1)I_1(|k_z|\rho_1)]C_1 + [AK_0(|k_z|\rho_1)K_1(|k_z|\rho_1)]C_2 \ , \text{ and} \tag{A.82}$$

$$C_4 = [AI_0(|k_z|\rho_1)I_1(|k_z|\rho_1)]C_1 + [1 - AI_0(|k_z|\rho_1)K_1(|k_z|\rho_1)]C_2 \ , \tag{A.83}$$

where $A = (1 - 1/\mu_{21})|k_z|\rho_1$. Similarly, using equations (A.77) and (A.79), and solving for C_3 and C_4, we obtain:

$$C_3 = [BK_0(|k_z|\rho_2)K_1(|k_z|\rho_2)]C_6 \ , \text{ and} \tag{A.84}$$

$$C_4 = [1 - BI_0(|k_z|\rho_2)K_1(|k_z|\rho_2)]C_6 \ , \tag{A.85}$$

where $B = (1-\mu_{32})|k_z|\rho_2$, and $\mu_{32} = \sigma_3/\sigma_2$. The system of equations (A.82), (A.83), (A.84), and (A.85) leads to the following solution for C_1:

$$C_1 = \frac{\begin{vmatrix} -AK_0(|k_z|\rho_1)K_1(|k_z|\rho_1)C_2 & -BK_0(|k_z|\rho_2)K_1(|k_z|\rho_2) \\ (1 - AI_0(|k_z|\rho_1)K_1(|k_z|\rho_1))C_2 & 1 - BI_0(|k_z|\rho_2)K_1(|k_z|\rho_2) \end{vmatrix}}{\begin{vmatrix} 1 - AK_0(|k_z|\rho_1)I_1(|k_z|\rho_1) & -BK_0(|k_z|\rho_2)K_1(|k_z|\rho_2) \\ -AI_0(|k_z|\rho_1)I_1(|k_z|\rho_1) & 1 - BI_0(|k_z|\rho_2)K_1(|k_z|\rho_2) \end{vmatrix}} \ . \tag{A.86}$$

Finally, by combining (A.72), (A.75), and (A.86), we obtain the explicit solution for the potential along the borehole.

B Extraction of Point Values from a Finite Element (FE) Solution.

Quantities of interest (q.o.i.) (4.37) and (4.38) represented in terms of point values are not continuous functionals in the energy space. Consequently, convergence in energy *does*

not imply convergence of point values. Additionally, since the q.o.i. functionals represent the load of the dual problem, the solution of the dual problem has infinite energy and the convergence analysis cannot be performed in the energy-norm. Because our *hp*-adaptive algorithm is based on minimizing interpolation errors measured in the energy-norm, solutions to both primal and dual problems should exhibit finite energy.

One way to avoid the problem with the q.o.i defined in terms of point values, is to modify the q.o.i. This can be achieved by considering finite-size antennas. After all, the induced current is measured with finite-size antennas. An alternative solution that avoids determining the (finite) size of the antennas consists of using a mathematical post-processing.

The idea of mathematical post-processing is to replace the original q.o.i. with a *continuous* functional coinciding with the original one for a class of functions that includes the solution of our problem. The new functional can then be evaluated for the FE solution. Because the FE solution converges to the exact one in the energy-norm, the post-processed value will converge to the exact value with the same convergence rates. Intuitively, fast convergence in energy is translated into fast convergence of q.o.i.

The extraction (post-processing) formulas proposed by Babuška and Miller [3, 4], constructed for elliptic problems with piecewise constant material data, perfectly suit our goals.

Let $S_\epsilon = S_\epsilon(\mathbf{x})$ be a ball of radius ϵ centered at $\mathbf{x}$. Let Ω_x be a subdomain of Ω with constant materials coefficients, and such that $S_\epsilon \subseteq \Omega_x$. Using Green's first identity, we obtain:

$$\int_{\Omega_x - S_\epsilon} \nabla u \nabla \xi \; dV = -\int_{\Omega_x - S_\epsilon} \Delta u \xi \; dV + \int_{\partial S_\epsilon} \frac{\partial u}{\partial n} \xi \; dS + \int_{\partial \Omega_x} \frac{\partial u}{\partial n} \xi \; dS \; , \tag{B.87}$$

where $\mathbf{n}$ is the unit normal outward vector. By interchanging u and ξ in the last equation, we obtain:

$$\int_{\Omega_x - S_\epsilon} \nabla \xi \nabla u \; dV = -\int_{\Omega_x - S_\epsilon} \Delta \xi u \; dV + \int_{\partial S_\epsilon} \frac{\partial \xi}{\partial n} u \; dS + \int_{\partial \Omega_x} \frac{\partial \xi}{\partial n} u \; dS \; . \tag{B.88}$$

By subtracting (B.88) from (B.87), we derive Green's second identity, namely,

$$0 = \int_{\Omega_x - S_\epsilon} \Delta \xi u - \Delta u \xi \; dV + \int_{\partial S_\epsilon} \frac{\partial u}{\partial n} \xi - \frac{\partial \xi}{\partial n} u dS + \int_{\partial \Omega_x} \frac{\partial u}{\partial n} \xi - \frac{\partial \xi}{\partial n} u dS \; . \tag{B.89}$$

Next, we select $\xi = \xi_F + \xi_0$, where ξ_F is the fundamental solution of problem $\Delta u = \delta(\mathbf{x})$ on Ω_x, and ξ_0 is a smooth cut-off function such that $\xi_0|_{\partial\Omega_x} = -\xi_F|_{\partial\Omega_x}$, and $\dfrac{\partial \xi_0}{\partial n}|_{\partial\Omega_x} = -\dfrac{\partial \xi_F}{\partial n}|_{\partial\Omega_x}$. Using the definition of ξ_0, yields:

$$\int_{\partial \Omega_x} \frac{\partial u}{\partial n} \xi \; dS = \int_{\partial \Omega_x} \frac{\partial \xi}{\partial n} u \; dS = 0 \; . \tag{B.90}$$

Also, since ξ_0 is smooth and ξ_F is the fundamental solution of the Laplace operator in $\mathbb{R}^3$, we obtain (using spherical coordinates)

$$\int_{\partial S_\epsilon} \frac{\partial u}{\partial n}\xi \; dS = \int_{\partial S_\epsilon} \frac{\partial u}{\partial n}(\frac{1}{4\pi\epsilon} + \xi_0)\epsilon^2 \; sin(\theta) \; d\theta d\phi \xrightarrow{\epsilon\to 0} 0 \; , \tag{B.91}$$

$$\begin{aligned}\int_{\partial S_\epsilon} \frac{\partial \xi}{\partial n} u \; dS = &\int_{\partial S_\epsilon} \frac{1}{4\pi\epsilon^2} u\epsilon^2 sin(\theta) \; d\theta d\phi \\ &+ \int_{\partial S_\epsilon} \frac{\partial \xi_0}{\partial n} u\epsilon^2 sin(\theta) \; d\theta d\phi \xrightarrow{\epsilon\to 0} u(\mathbf{x}) + 0 = u(\mathbf{x}) \; .\end{aligned} \tag{B.92}$$

Since u is the FE solution of equation (2.7) with $\nabla \cdot \mathbf{J} = 0$, we have that $\Delta u|_{\Omega_x} \approx 0$. Also, $\Delta \xi_F|_{\Omega_x - S_\epsilon} = 0$. Then, we obtain

$$\int_{\Omega_x - S_\epsilon} \Delta\xi u \; dV = \int_{\Omega_x - S_\epsilon} \Delta\xi_0 u \; dV \xrightarrow{\epsilon\to 0} \int_{\Omega_x} \Delta\xi_0 u \; dV \; , \tag{B.93}$$

$$\int_{\Omega_x - S_\epsilon} \Delta u\xi \; dV \approx 0. \tag{B.94}$$

By substituting (B.90), (B.91), (B.92), (B.93), and (B.94), into (B.89) we conclude that

$$u(\mathbf{x}) = \int_{\Omega_x} \Delta\xi_0 u \; dV = 2\pi \int_{\Omega_x} \Delta\xi_0 u \; \rho \; d\rho dz \; . \tag{B.95}$$

This post-processing formula is only valid for functions u such that $\Delta u = 0$ in Ω_x.

It still remains necessary to construct a smooth function ξ_0 such that $\xi_0|_{\partial\Omega_x} = -\xi_F|_{\partial\Omega_x}$, and $\frac{\partial \xi_0}{\partial n}|_{\partial\Omega_x} = -\frac{\partial \xi_F}{\partial n}|_{\partial\Omega_x}$. This function ξ_0 is not unique. Several techniques can be used to construct it. For example, we can use transfinite interpolation with Hermite blending functions [22]. To illustrate this, we show the construction of ξ_0 for a 2D unit square domain $\Omega_x = [0,1]^2$.

Hermite Interpolation. We define the following Hermite Interpolation polynomials defined in the unit interval $s \in [0,1]$:

$$\begin{aligned} h_1^s &= h_1(s) = 2s^3 - 3s^2 + 1 \; , \\ h_2^s &= h_2(s) = s^3 - 2s^2 + s \; , \\ h_3^s &= h_3(s) = -2s^3 + 3s^2 \; , \text{ and} \\ h_4^s &= h_4(s) = s^3 - s^2 \; . \end{aligned} \tag{B.96}$$

These cubic polynomials exhibit the following properties:

$$\begin{aligned}
&h_1(0) = 1 \;\;;\;\; h_2(0) = 0 \;\;;\;\; h_3(0) = 0 \;\;;\;\; h_4(0) = 0 \quad , \\
&h_1'(0) = 0 \;\;;\;\; h_2'(0) = 1 \;\;;\;\; h_3'(0) = 0 \;\;;\;\; h_4'(0) = 0 \quad , \\
&h_1(1) = 0 \;\;;\;\; h_2(1) = 0 \;\;;\;\; h_3(1) = 1 \;\;;\;\; h_4(1) = 0 \quad , \\
&h_1'(1) = 0 \;\;;\;\; h_2'(1) = 0 \;\;;\;\; h_3'(1) = 0 \;\;;\;\; h_4'(1) = 1 \quad .
\end{aligned} \tag{B.97}$$

Let $\mathbf{p_1}$, $\mathbf{p_2}$, $\mathbf{p_3}$, and $\mathbf{p_4}$ be the four corner points of the 2D unit square. Then, we construct the following bi-cubic polynomials:

$$\begin{aligned}
u_b^1(x,y) &= \xi_F(\mathbf{p_1})h_1^x h_1^y + \frac{\partial \xi_F}{\partial x}(\mathbf{p_1})h_2^x h_1^y + \frac{\partial \xi_F}{\partial y}(\mathbf{p_1})h_1^x h_2^y + \frac{\partial^2 \xi_F}{\partial x \partial y}(\mathbf{p_1})h_2^x h_2^y \;, \\
u_b^2(x,y) &= \xi_F(\mathbf{p_2})h_3^x h_1^y + \frac{\partial \xi_F}{\partial x}(\mathbf{p_2})h_4^x h_1^y + \frac{\partial \xi_F}{\partial y}(\mathbf{p_2})h_3^x h_2^y + \frac{\partial^2 \xi_F}{\partial x \partial y}(\mathbf{p_2})h_4^x h_2^y \;, \\
u_b^3(x,y) &= \xi_F(\mathbf{p_3})h_3^x h_3^y + \frac{\partial \xi_F}{\partial x}(\mathbf{p_3})h_4^x h_3^y + \frac{\partial \xi_F}{\partial y}(\mathbf{p_3})h_3^x h_4^y + \frac{\partial^2 \xi_F}{\partial x \partial y}(\mathbf{p_3})h_4^x h_4^y \;, \\
u_b^4(x,y) &= \xi_F(\mathbf{p_4})h_1^x h_3^y + \frac{\partial \xi_F}{\partial x}(\mathbf{p_4})h_2^x h_3^y + \frac{\partial \xi_F}{\partial y}(\mathbf{p_4})h_1^x h_4^y + \frac{\partial^2 \xi_F}{\partial x \partial y}(\mathbf{p_4})h_2^x h_4^y \;, \\
u_b(x,y) &= u_b^1(x,y) + u_b^2(x,y) + u_b^3(x,y) + u_b^4(x,y) \;.
\end{aligned} \tag{B.98}$$

Now, let $\mathbf{e_1}$, $\mathbf{e_2}$, $\mathbf{e_3}$, and $\mathbf{e_4}$ be the four edges of the 2D unit square. We define:

$$\begin{aligned}
u_e^1(x,y) &= (\xi_F - u_b)|_{\mathbf{e_1}} h_1^y + (\frac{\partial \xi_F}{\partial y} - \frac{\partial u_b}{\partial y})|_{\mathbf{e_1}} h_2^y \;, \\
u_e^2(x,y) &= (\xi_F - u_b)|_{\mathbf{e_2}} h_3^x + (\frac{\partial \xi_F}{\partial x} - \frac{\partial u_b}{\partial x})|_{\mathbf{e_2}} h_4^x \;, \\
u_e^3(x,y) &= (\xi_F - u_b)|_{\mathbf{e_3}} h_3^y + (\frac{\partial \xi_F}{\partial y} - \frac{\partial u_b}{\partial y})|_{\mathbf{e_3}} h_4^y \;, \\
u_e^4(x,y) &= (\xi_F - u_b)|_{\mathbf{e_4}} h_1^x + (\frac{\partial \xi_F}{\partial x} - \frac{\partial u_b}{\partial x})|_{\mathbf{e_4}} h_2^x \;, \\
u_e(x,y) &= u_e^1(x,y) + u_e^2(x,y) + u_e^3(x,y) + u_e^4(x,y) \;.
\end{aligned} \tag{B.99}$$

Finally, $\xi_0(x,y) = -(u_b(x,y) + u_e(x,y))$ has the following properties:

$$\xi_0|_{\partial\Omega} = -\xi_F|_{\partial\Omega} \quad ; \quad \frac{\partial \xi_0}{\partial n}|_{\partial\Omega} = -\frac{\partial \xi_F}{\partial n}|_{\partial\Omega} \;, \tag{B.100}$$

and $\xi_0(x,y)$ is smooth ($\xi_0 \in C^2(\Omega)$).

C Comparative results

In this appendix, we describe a comparative study based on numerical experimentation of different adaptive strategies for the case when a particular feature of the solution is pursued. More precisely, we are interested in minimizing the error of the FE solution evaluated at a specific point. Typically, special averaging functions (called *mollifiers*) are used to define a continuous linear functional $L \in V'$ utilized as the quantity of interest (see [16]) to be minimized. Also, special post-processing techniques may be used, as the one presented in Section B. In this appendix, for simplicity, we define the following quantity of interest:

$$L(e) = \frac{1}{|\Omega_i|} \int_{\Omega_i} e(x) dx \ , \tag{C.101}$$

where Ω_i is a small subdomain containing the target point x_i where an approximation of the solution is desired.

Two elliptic problems are used to perform this numerical study: an L-shape domain problem, and an orthotropic heat conduction problem in a thermal battery. For each model problem, we describe the geometry, governing equations, material coefficients, and boundary conditions. We also display the exact or approximate solution, and we briefly explain the relevance of each problem in this research. Then, based on these two problems, we describe results obtained by comparing different adaptive strategies.

C.1 L-Shape Domain Problem

We want to solve Laplace equation ($-\Delta u = 0$) with essential (Dirichlet) BC (possibly, non-homogeneous) corresponding to the exact solution $u = r^{2/3} sin(2\theta/3 + \pi/3)$, expressed in terms of cylindrical coordinates. The geometry ($[-1, 0] \times [0, 1] + [0, 1] \times [0, 1] + [0, 1] \times [-1, 0]$) of the computational domain along with the exact solution are displayed in Fig. 11.

This problem has a reentrant corner located at the origin, thereby producing a singularity on the solution. We are interested in the FE solution at the proximity of the point $(-1/2, 1/2)$. We select the functional L given by (C.101) with $\Omega_i = [-0.5625, -0.4375] \times [0.4375, 0.5625]$ as our quantity of interest.

Fig. 12 displays the convergence history for both the pointwise error and the quantity of interest error, yielded by different self-adaptive algorithms. Fig. 13 describes the convergence

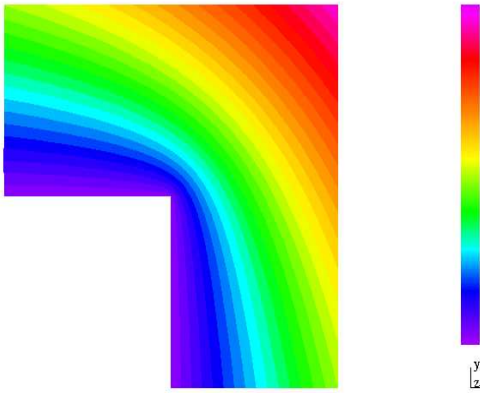

Figure 11: Exact solution of the L-shape domain problem

history of the upper bound U of $\mid E \mid$, given by

$$\begin{cases} h\text{-goal: } U = \sum\limits_K \mid u - u_{hp} \mid^2_{1,K} \\ hp\text{-goal 1 (3.29): } U = \sum\limits_K \mid \mid (u+w) - \Pi^K_{hp}(u+w) \mid^2_{1,K} \\ \qquad\qquad\qquad - \mid (u-w) - \Pi^K_{hp}(u-w) \mid^2_{1,K} \mid \\ hp\text{-goal 2 (3.30): } U = \sum\limits_K \mid u - \Pi^K_{hp} u \mid_{1,K} \cdot \mid w - \Pi^K_{hp} w \mid_{1,K} \quad . \end{cases} \tag{C.102}$$

Final hp-grids for different self-adaptive algorithms are shown in Figures 14, and 15.

C.2 Orthotropic Heat Conduction Battery

We present now a benchmark problem proposed by Sandia[3], in which we solve the heat equation in a thermal battery with large and *orthotropic* jumps in the material coefficients (up to six orders of magnitude). The Geometry ($[0, 8.4] \times [0, 24]$) of the computational domain along with an approximation of the unknown exact solution are displayed in Fig. 16.

This problem is governed by the heat conduction equation $\nabla(\mathbf{K}\nabla u) = f^{(k)}$, where $\mathbf{K}$ is given by:

$$\mathbf{K} = \mathbf{K}^{(k)} = \begin{bmatrix} K_x^{(k)} & 0 \\ 0 & K_y^{(k)} \end{bmatrix} . \tag{C.103}$$

[3]Sandia National Laboratories, USA

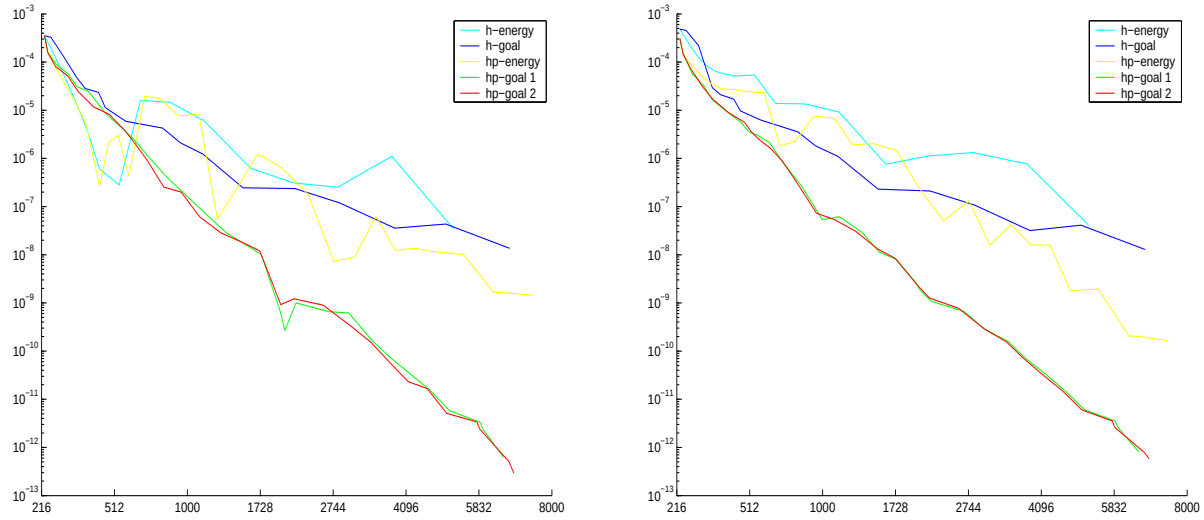

Figure 12: L-shape domain problem. Pointwise convergence (left panel) and convergence of quantity of interest $\mid L(e) \mid$ (right panel) obtained using different automatic refinement strategies. 'hp-goal 1' and 'hp-goal 2' correspond to *hp*-algorithms (3.29) and (3.30) respectively.

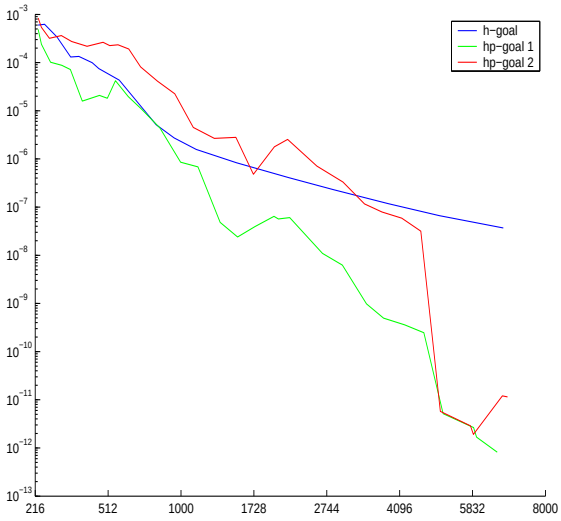

Figure 13: L-shape domain problem. Convergence history of the upper bound U of $\mid E \mid$ corresponding to different goal-oriented algorithms.

For each material k, we define:

$$f^{(k)} = \begin{cases} 0, & \text{k=1} \\ 1, & \text{k=2} \\ 1, & \text{k=3} \\ 0, & \text{k=4} \\ 0, & \text{k=5} \end{cases} \quad K_x^{(k)} = \begin{cases} 25, & \text{k=1} \\ 7, & \text{k=2} \\ 5, & \text{k=3} \\ 0.2, & \text{k=4} \\ 0.05, & \text{k=5} \end{cases} \quad K_y^{(k)} = \begin{cases} 25, & \text{k=1} \\ 0.8, & \text{k=2} \\ 0.0001, & \text{k=3} \\ 0.2, & \text{k=4} \\ 0.05, & \text{k=5} \end{cases} . \tag{C.104}$$

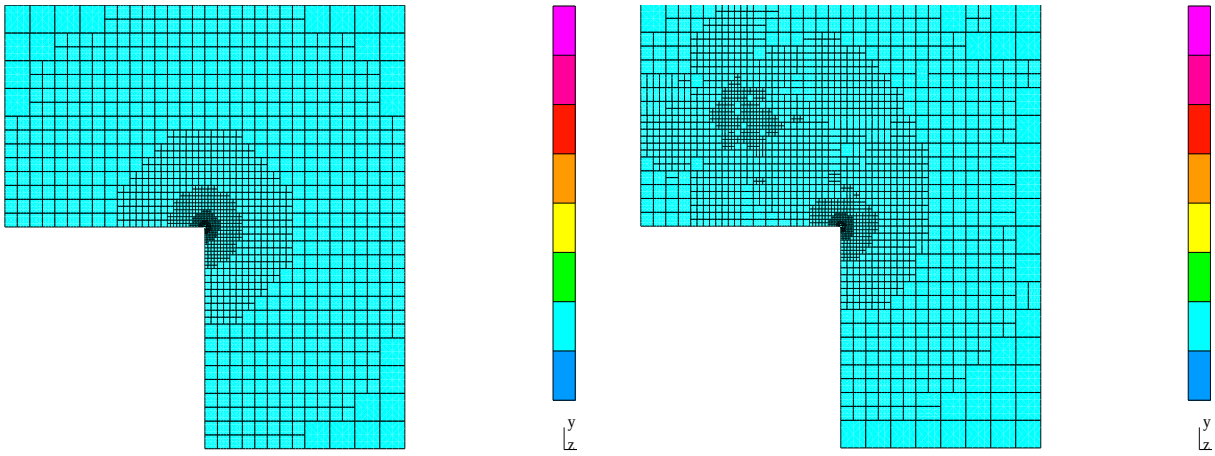

Figure 14: L-shape domain problem. Final h-grids containing 5177 (left panel) and 6691 (right panel) unknowns (degrees of freedom) obtained with the fully automatic energy norm based (left panel) and goal-oriented based (right panel) h-adaptive algorithms.

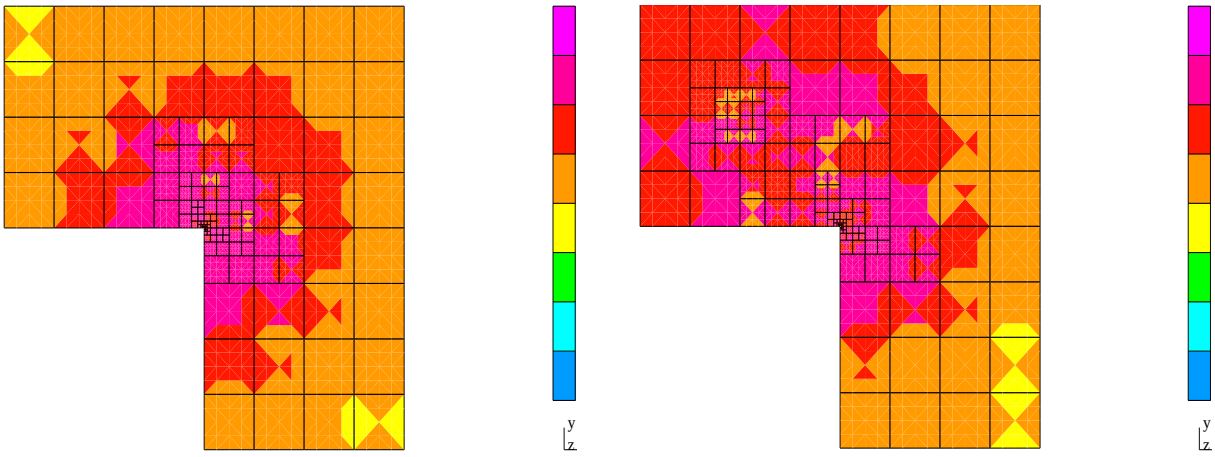

Figure 15: L-shape domain problem. Final hp-grids containing 7392 (left panel) and 6815 (right panel) unknowns (degrees of freedom) obtained with the fully automatic energy norm based (left panel) and goal-oriented based (right panel) hp-adaptive algorithms. Different colors indicate different polynomial orders of approximation, ranging from 1 (blue) to 8 (pink).

By ordering the four sides of the boundary clockwise, and by starting with the left-hand side boundary, we impose the following boundary conditions:

$$\mathbf{K}\nabla u \cdot n = g^{(i)} - \alpha^{(i)} u \, , \tag{C.105}$$

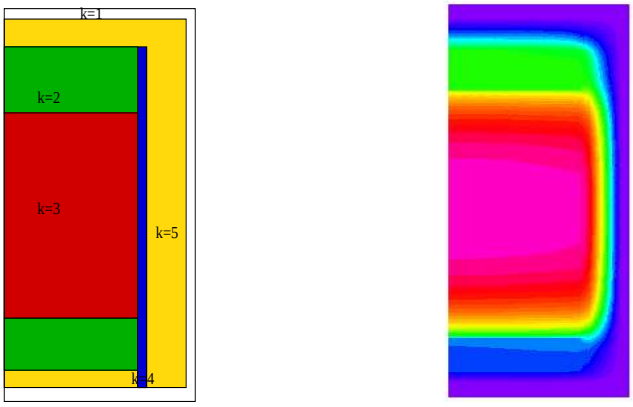

Figure 16: Geometry (left panel) and FE solution (right panel) of the orthotropic heat conduction problem in a thermal battery.

where

$$\alpha^{(i)} = \begin{cases} 0, & \text{i=1} \\ 1, & \text{i=2} \\ 2, & \text{i=3} \\ 3, & \text{i=4} \end{cases} \qquad g^{(i)} = \begin{cases} 0, & \text{i=1} \\ 3, & \text{i=2} \\ 2, & \text{i=3} \\ 0, & \text{i=4} \end{cases} . \tag{C.106}$$

This problem exhibits several singularities of different strength. We are interested in the FE solution in the proximity of point $(8.2, 0.4)$, located at the southeast part of the domain. More precisely, we select the functional L given by (C.101) with $\Omega_i = [8.0, 8.4] \times [0.0, 0.8]$ as the quantity of interest.

Fig. 17 shows the convergence history of the pointwise error and the quantity of interest error for different self-adaptive algorithms. Fig. 18 shows the convergence history of the upper bound U of $\mid E \mid$, given by (C.102).

Final *hp*-grids (and their amplifications) for different self-adaptive algorithms are displayed in Figures 19, 20, 21, and 22.

C.3 Conclusions from This Appendix:

From the comparative numerical study described above, we conclude the following:

- When a particular feature of the solution is desired, goal-oriented adaptivity delivers significantly better results than energy-norm based adaptivity. In addition, as the ratio

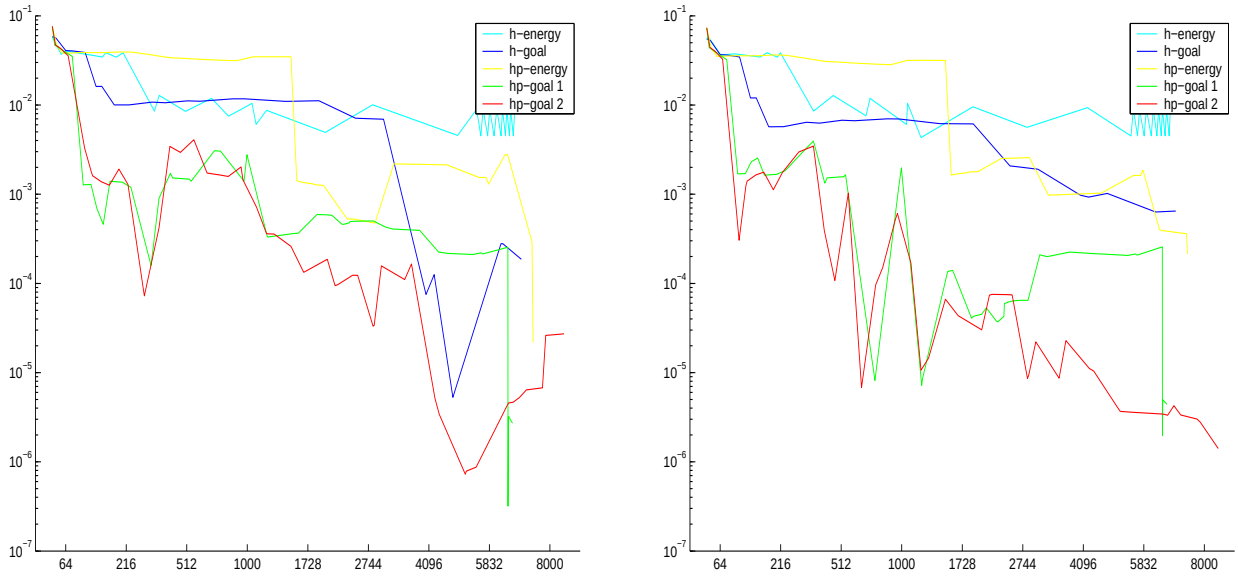

Figure 17: Orthotropic heat conduction problem. Pointwise convergence (left panel) and convergence of quantity of interest $\mid L(e) \mid$ (right panel) obtained using different automatic refinement strategies. *hp-goal 1* and *hp-goal 2* correspond to *hp*-algorithms (3.29) and (3.30), respectively.

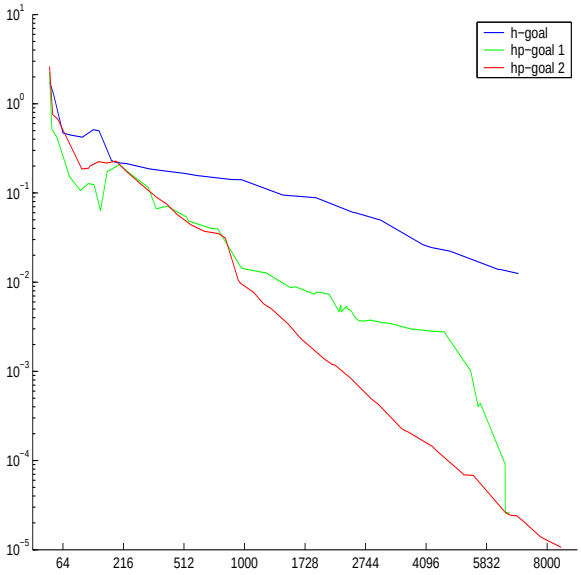

Figure 18: Orthotropic heat conduction problem. Convergence history of the upper bound U of $\mid E \mid$ corresponding to different goal-oriented algorithms.

between the value of the *quantity of interest* and the energy of the solution increases, the more essential becomes the use of goal-oriented algorithms.

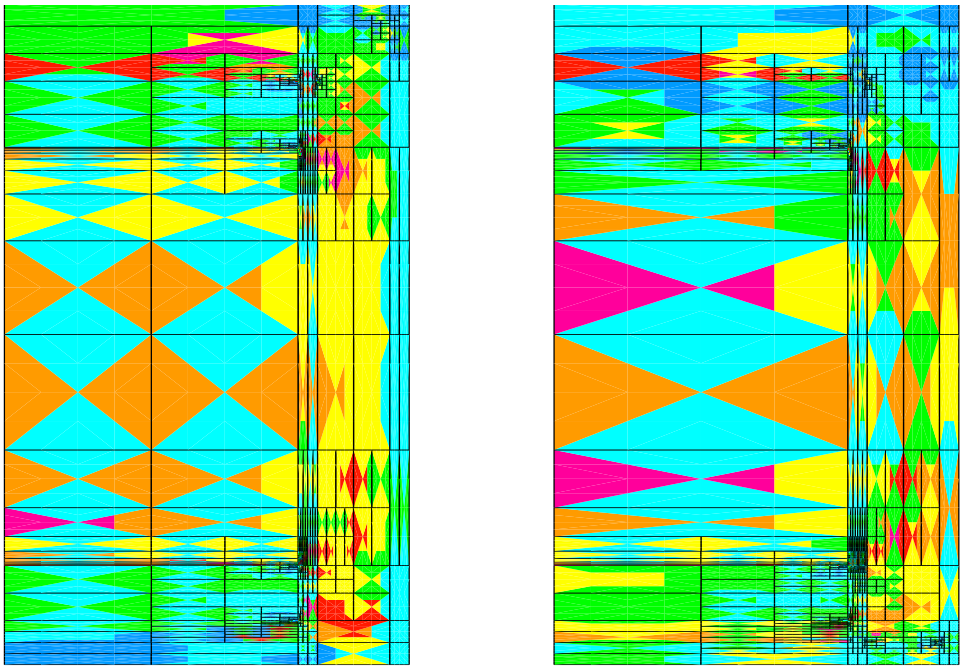

Figure 19: Orthotropic heat conduction problem. Final *hp*-grids containing 7353 (left panel) and 6605 (right panel) unknowns (degrees of freedom) obtained with the fully automatic energy-norm based (left panel) and goal-oriented based (right panel) *hp*-adaptive algorithms. Different colors indicate different polynomial orders of approximation, ranging from 1 (blue) to 8 (pink).

- Since convergence of *hp*-adaptive methods is exponential (as opposed to algebraic convergence of *h*-adaptive methods), results obtained with *hp*-adaptive algorithms are considerably more accurate than results obtained with *h*-adaptive algorithms.
- The two goal-oriented *hp*-adaptive algorithms considered in this paper (3.29), and (3.30) provide similar results.

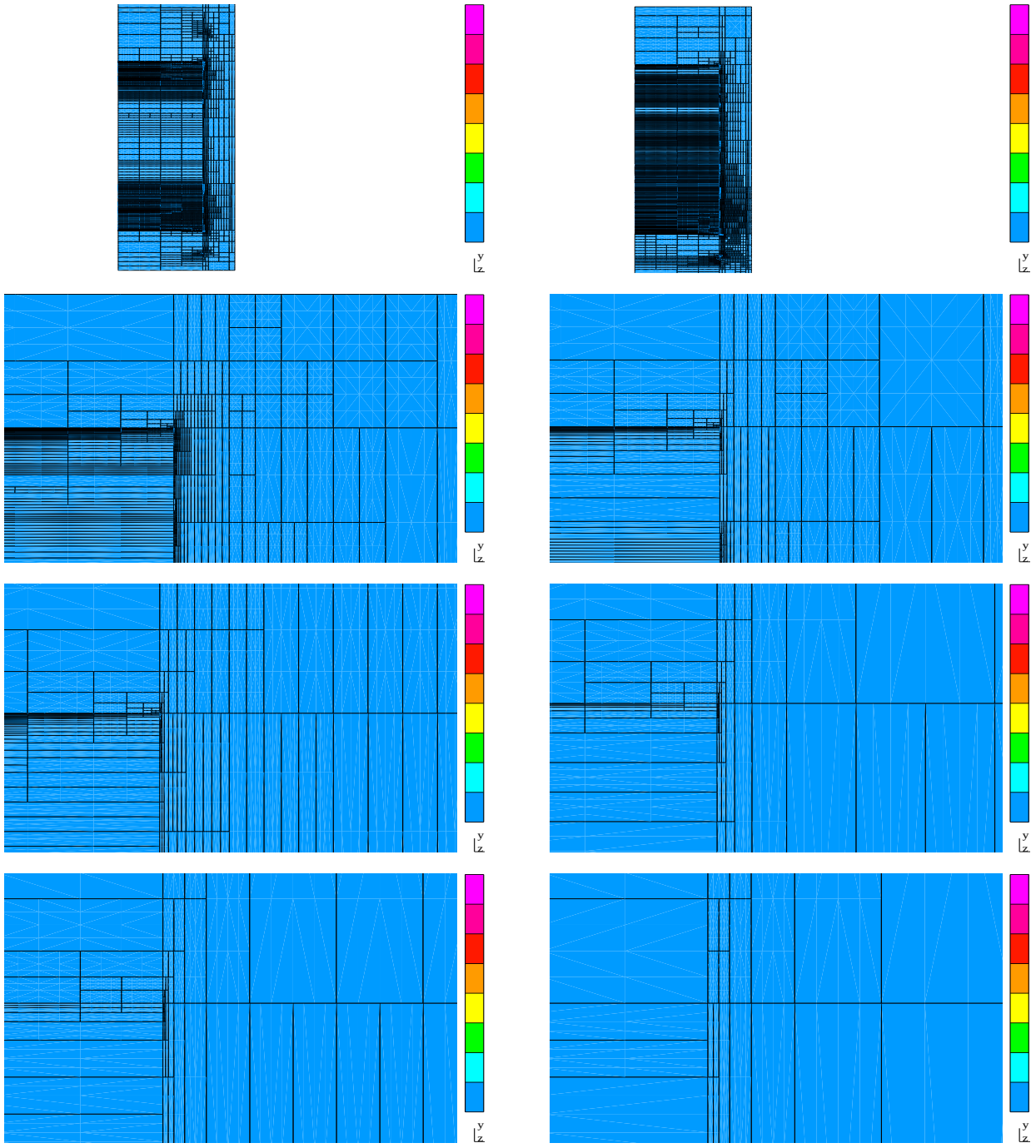

Figure 20: Orthotropic heat conduction problem. Progressive amplifications toward a singularity located at point $(18.8, 6.1)$ by factors of 1, 10, 100, and 10000 (from top to bottom) of the final h-grids obtained with the fully automatic energy norm based (left panel) and goal-oriented based (right panel) h-adaptive algorithms.

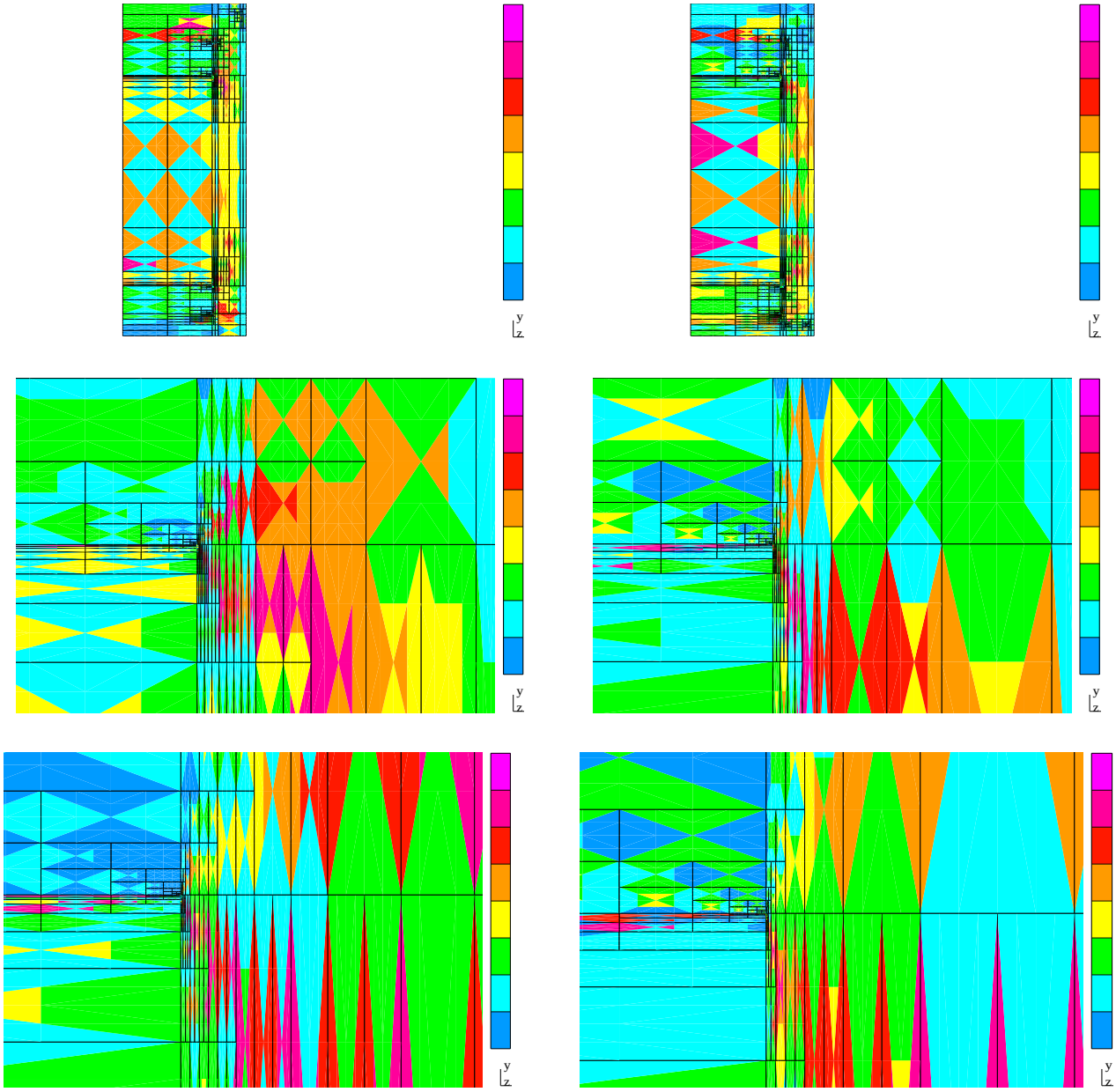

Figure 21: Orthotropic heat conduction problem. Progressive amplifications toward a singularity located at point $(18.8, 6.1)$ by factors of 1 (top), 10 (middle), and 100 (bottom) of the final *hp*-grids obtained with the fully automatic energy norm based (left panel) and goal-oriented based (right panel) *hp*-adaptive algorithms. Different colors indicate different polynomial orders of approximation, ranging from 1 (blue) to 8 (pink).

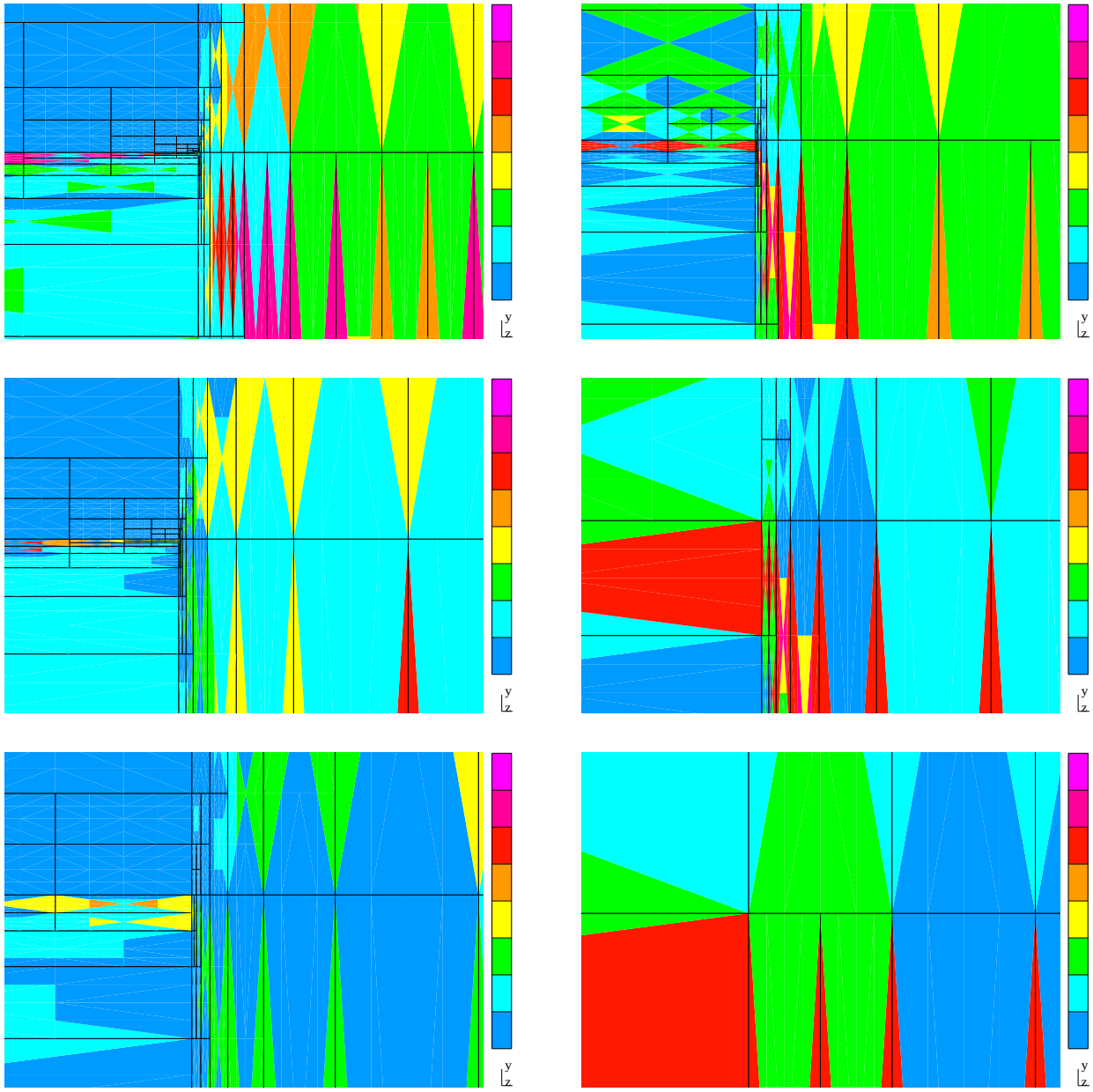

Figure 22: Orthotropic heat conduction problem. Progressive amplifications toward a singularity located at point $(18.8, 6.1)$ by factors of 1000 (top), 10000 (middle), and 100000 (bottom) of the final *hp*-grids obtained with the fully automatic energy norm based (left panel) and goal-oriented based (right panel) *hp*-adaptive algorithms. Different colors indicate different polynomial orders of approximation, ranging from 1 (blue) to 8 (pink).